

NIKA2 research note

NIKA2 COMMISSIONING RESULTS V1.0

NIKA2 team
NIKA2 collaboration
June 27, 2017

Contents

1	Introduction	3
1.1	Commissioning goals	3
1.2	Commissioning runs	3
2	Bandpasses	3
3	Opacity derivation	4
4	Focal Plane Reconstruction	6
4.1	Methodology	6
4.2	Average Focal Plane Reconstruction	9
5	Pointing accuracy	11
6	Beam pattern	11
6.1	Optimal focus	11
6.1.1	Focus estimation	16
6.1.2	Reconstruction of the focus surfaces	16
6.1.3	Constraints on the X and Y foci	20
6.2	Full beam pattern	20
6.2.1	Data sets	20
6.2.2	Deep beam maps	25
6.2.3	Beam profile	27
6.3	Main beam	27
6.3.1	Sidelobe-masked Profile-based analysis	27
6.3.2	Sidelobe-masked Map-based analysis	27
6.4	Beam efficiency	28
6.5	Stability of the beam pattern	28

7 Calibration	29
7.1 NIKA2 Photometric System	29
7.1.1 Response of a detector to astronomical source	29
7.1.2 Effect of the atmosphere	30
7.1.3 Beammap of a calibrator	32
7.1.4 Calibration in FWHM ₀ beam	32
7.1.5 Color correction for point sources measured with fixed gaussian fit	34
7.1.6 Calibration for aperture photometry	34
7.1.7 Calibration in surface brightness	34
7.2 Reference flux densities of the calibrators	34
7.2.1 Uranus and Neptune	35
7.2.2 Mars	36
7.2.3 Secondary calibrators: asteroids	36
7.3 Aperture photometry	38
7.4 Stability of the flux density scale with the primary calibrators Uranus and Neptune	40
7.5 Stability of the flux density scale with three secondary calibrators	41
7.6 Calibration stability across the run	42
8 Noise description: TOI and maps	42
8.1 Dark detectors at 1 mm	42
8.2 Dark tests	42
9 Detector-Detector correlation matrix	42
9.1 RMS of the noise	43
9.2 Discussion	44
10 Sensitivities	45
10.1 Data processing	45
10.2 NEFD Methods 1 and 2: deep integration	45
10.3 NEFD Method 3: scan NEFD vs opacity and air mass	45
11 Summary of performance	46
A Reference to technical documentation	46
A.1 Consortium-lead documentation	47
A.2 IRAM-lead documentation	47

Abstract

This notes describe the main results of the NIKA2 commissioning campaigns.

1 Introduction

1.1 Commissioning goals

The main goal of the NIKA2 commissioning runs described below is to characterize the instrument and check its performances with respect to the specifications described in Table 1. We also characterize the performance stability against various observing conditions and assess the precision with which the performance parameter are measured.

Table 1: Main characteristics defining the expected performances of NIKA2. Each parameter  associated with two values: the first one indicates the *specifications*, i.e. the requirements to be met by the instrument, while the second bracketed one gives the *goals*, i. e. the values targeted by the collaboration.

Reference Wavelength [mm]	1.2	2.0
Reference Frequency [GHz]	260	150
FOV diameter [arcmin]	5 (6.5)	5 (6.5)
Pixel size in beam sampling unit [$F\lambda$]	0.9 (0.6)	0.9 (0.6)
FWHM [arcsec]	12 (10)	18 (16)
Fraction of valid detectors [%]	50 (90)	50 (90)
NEFD ^a [$\text{mJy} \cdot \text{s}^{1/2} / \text{beam}$]	30 (15)	20 (10)
NEFD [$\text{mJy} \cdot \text{s}^{1/2} / \text{beam}$] goal on 90% of the pixels	15	10
NEFD [$\text{mJy} \cdot \text{s}^{1/2} / \text{beam}$] specification on 50% of the pixels	30	20

^(a) NEFD in typical IRAM good sky opacity condition: 2mm pwv, 60° elevation

1.2 Commissioning runs

We had 10 commissioning runs for NIKA2 as described in Table 3.

2 Bandpasses

The NIKA2 spectral bands were measured in the laboratory using a Martin Pupplet interferometer. Both arrays and filter bands were considered in the measurements. These were obtained from the difference of two black-bodies, hence they include  $a \propto \nu^2$ RJ term. During the commissioning in Run 5 array 2 was replaced. The new array has a different spectral transmission.  Figure shows the spectral transmissions for the three arrays. Notice that array A2 was replaced by a new  in N2R5 and that the spectral transmissions are not the same (red and cyan lines in the figure).

Table 2: Commissioning campaigns, dates and general comments.

RUN	NIKA Run	Starting date	End date	General comments
N2R1	13	29-October-2015	10-November-2015	Not full instrumentation
N2R2	14	24-November-2015	02-December-2015	13 NIKEI boards working
N2R3	15	12-January-2016	01-February-2016	20 NIKEI boards
N2R4	16	1-March-2016	15-March-2016	
Dark run	17	4-May-2016	4-May-2016	Dark tests with N2R4 conditions
N2R5	18	16-September-2016	11-October-2016	New dichroic, corrugated lenses, new array 2 mm, new electronics
N2R6	19	25-October-2016	1-November-2016	
N2R7	20	6-December-2016	13-December-2016	Test external calibrator
N2R8	21	9-January-2017	13-January-2017	Replace array 1 lens by smooth 
N2R9	22	24-January-2017	25-January-2017	Tests on the sky
N2R10	23	21-February-2017	28-February-2017	
N2R11	24	18-April-2017	25-April-2017	End of commisioning phase 1, Science verification
		8-June-2017	13-June-2017	polarization commissioning

Table 3: Spectral transmission characteristics for the NIKA2 arrays.

	A1	A3	A2 2015	A2 2016
Central Frequency [GHz]	255.5	257.8	147.7	151.6
Bandwidth [GHz]	47.8	45.7	41.8	42.1

Using the NIKA2 bandpasses for N2R9, we can integrate the ATM atmospheric model to compute the expected ratio between the atmospheric opacity for the two NIKA2 channels. This shown in Figure 2 where we present the atmospheric opacity ratio of the 2 and 1 mm channels as a function of the opacity for the 1 mm one. 

3 Opacity derivation

For each kid k , f_{tone}^k moves with the atmospheric load according to

$$f_{tone}^k = C_0^k + C_1^k T_{atm} [1 - e^{-\tau / \sin \delta}] \quad (1)$$

where δ is the elevation. The skydip procedure consists in moving the telescope in elevation step by step and to monitor, for each kid, the evolution of f_{tone}^k vs the air mass and to fit the opacity τ and C_0^k and C_1^k . All the skydips (that were obtained under various opacity conditions) are analysed together to break the degeneracies between these parameters. The procedure has two steps. First, all the skydips are analysed individually to simply measure f_{tone}^k for each stable elevation and fit simultaneously all the parameters. Error

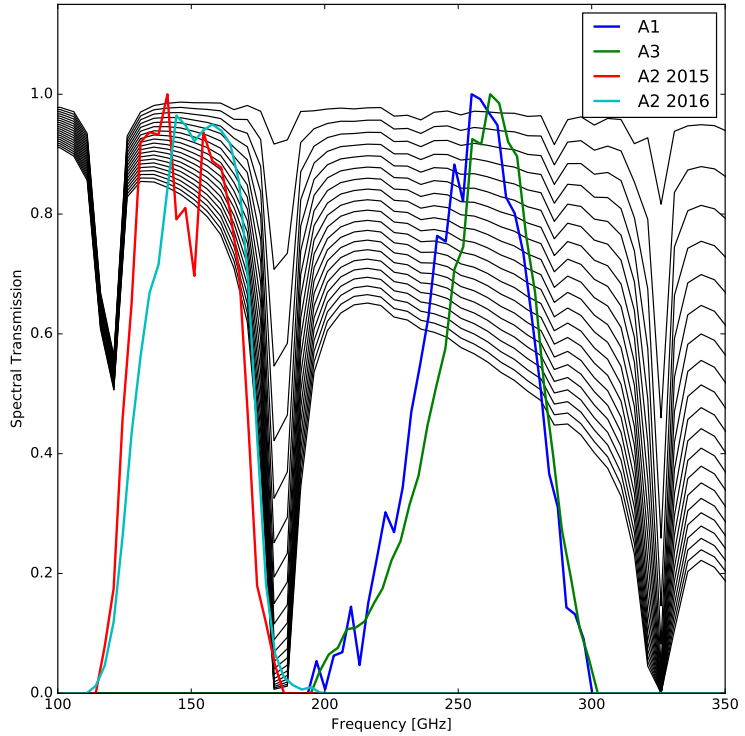


Figure 1: Spectral transmission of the three NIKA2 arrays as a function of frequency in GHz. For illustration we also plot the ATM atmospheric model for different values of pwv.

bars on τ are estimated by doing this procedure on blocks of 40 kids only and getting a dispersion on the resulting τ from the different blocks. Usually the dispersion comes out as 4×10^{-3} at 1mm and 1×10^{-3} at 2mm. Once the τ values are estimated for each skydip (as the average over the blocks), we compute (while fixing τ) the C_0 and C_1 final values for each kid. We thus retrieve the coefficients of all the Kids even though some of them could not contribute to the tau determination.

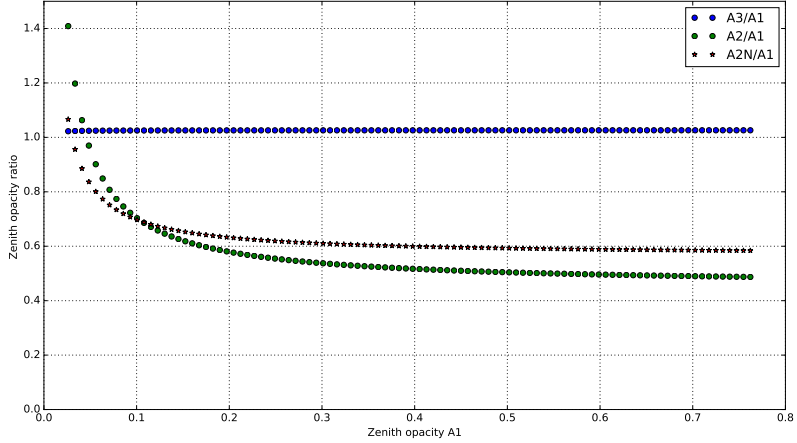


Figure 2: Expected atmospheric opacity ratio of the 2 and 1 mm channels as function of the opacity at 1 mm.

Array	Number of valid kids	Fraction of all kids
A1	793	0.75
A2	481	0.83
A3	872	0.83

4 Focal Plane Reconstruction

4.1 Methodology

In order to determine the pointing offsets of each KID w.r.t. the reference sky coordinates as commanded by the telescope tracking system, we perform a “beammap”, that is to say we map a bright and compact source, most of the time a planet, with a elevation step small enough to meet Nyquist sampling at the 1mm beam scale, namely 4.8 arcsec. We observe this planet with a raster scan in (az,el) coordinates, either with fixed elevation subscans or fixed azimuth subscans. The former has the advantage of low air mass variation across a subscan, the latter offers an orthogonal scan direction to the former: the combination of both gives a more accurate determination of the far side lobes. The data reduction proceeds in two steps.

Step 1. We apply a median filter per KID timeline whose width is 4 FWHM and we project one map per KID in Nasmyth coordinates. This median filter removes most of atmospheric and low frequency electronic noise efficiently,

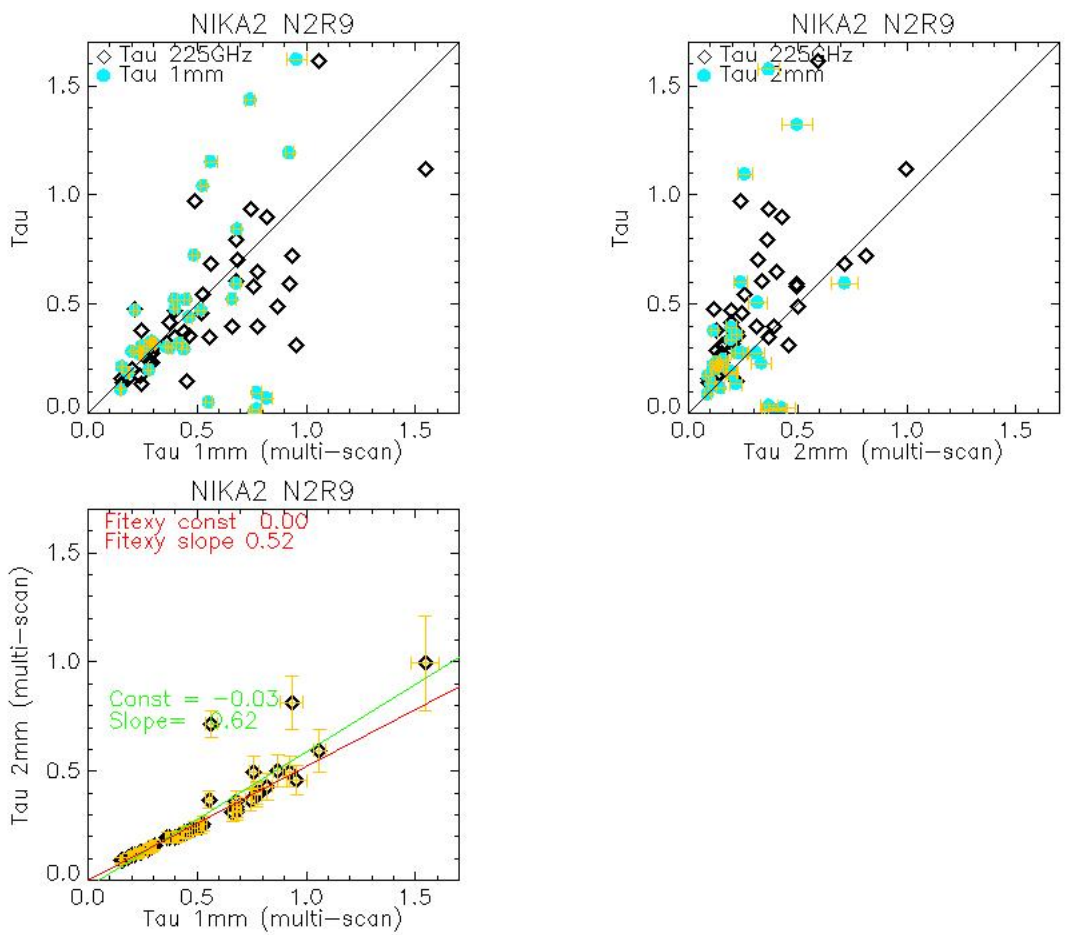


Figure 3: Fix me : improve plot quality and plot only the 3rd one.

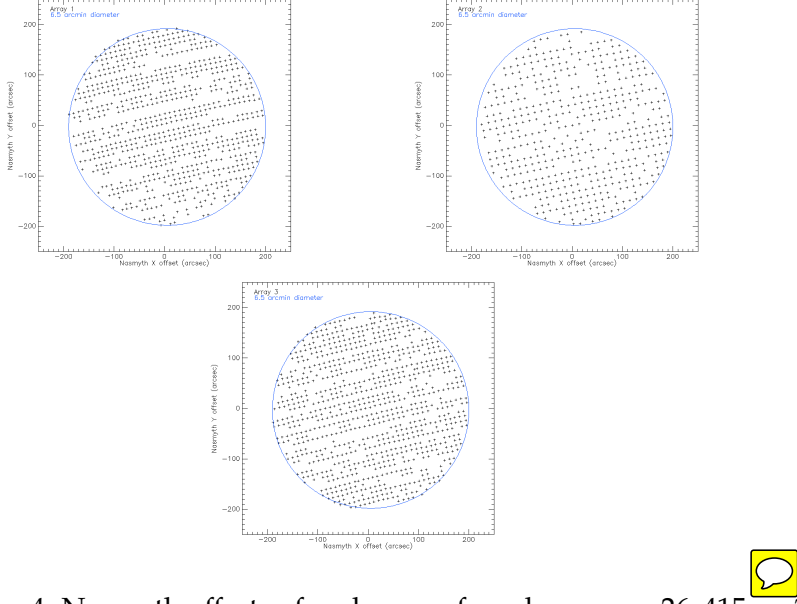


Figure 4: Nasmyth offsets of each array, from beammap 26s415 on 3C84.

albeit a slight ringing and flux loss on the source. However, at this stage, we are only interested in the location of the observed planet. To derive the Nasmyth coordinates from the provided (az,el) coordinates, we build the following quantities at each time t

$$\begin{aligned} dx_t &= \cos el_t daz_t - \sin el_t del_t \\ dy_t &= \sin el_t daz_t + \cos el_t del_t \end{aligned}$$

where el_t is the elevation of the reference pointing direction and daz and del are the pointing offsets w.r.t to the source in azimuth and elevation as provided by the tracking system. Note that daz is already corrected by the $\cos el_t$ factor to have orthonormal coordinates in the tangent plane of the sky and be immune to the geodesic convergence at the poles. We then fit a 2D elliptical gaussian on each KID map. The centroid of this gaussian is a first estimate of the KID offsets, FWHM's, ellipticity and sensitivity. We apply a first KID selection by removing outliers to the statistics on these parameters. We also discard manually KIDs that show a cross-talk counter part on their map. At the end of this first step, we are ready to move to a second stage.

Step 2. With the Nasmyth offsets derived in step 1, we are now able to mask out the planet in each KID timeline. This mask is centered on the

planet location as seen by each kid, it is circular and has a radius of 60 arcsec. We now build a template timeline (a.k.a. “common mode”) in two steps. First, we take the median of all samples of all KIDs that are outside this mask at a given time t . This gives a first estimate of the common mode. Second, we cross-calibrate each KID on this common mode when the KID is outside the mask and we coadd all these KID cross-calibrated timelines when they are outside the mask to have the final common mode. In this sum, each KID TOI is weighted by the inverse of its variance outside the mask. Once we have this common mode in hand, we cross-calibrate each TOI on it outside the mask and we subtract it to the entire KID TOI. When then resume to the projection of each KID TOI in Nasmyth coordinates like in step 1, and the 2D elliptical gaussian fit on the each kid map. The centroid coordinates and the FWHM are now the final parameters that can be derived on the current scan.

This analysis is repeated on all the beam maps, which provides statistics and precision on each KID parameter, together with estimates on KID performance stability.

show a screen capture of Katana.

$$FOVdiameter = \sqrt{4N_{tot.kids} * gridstep^2 / \pi} \quad (2)$$

The same definition applies to “Effective FOV” to avoid extra multiplication by the fraction of valid pixels

$$F\lambda = gridstep \times D(30m) / \lambda \quad (3)$$

4.2 Average Focal Plane Reconstruction

In order to identify the most stable pixels, we compare the KIDs parameter obtained with several beam maps. In the following we will show results as obtained using seven beam maps from Run10, two from Run9 and one from Run8. For each pixel we compute the average position on the focal plane and the average FWHM, counting the times that it has been considered as valid.

In Fig. 5 we show the average focal plane reconstruction, from green to red depending on the number of times that the pixel has been considered as valid. For A1, A3 and A2, respectively, we have 952, 961, and 553 pixels that have been considered as valid at least twice (840, 508, 868 valid at least five times). As a second step, we also flag pixels that move across the focal plane from a beam map to another (Fig. 6 , jumping KIDs) and those who share the same position (twin KIDs). To identify the former we look at the

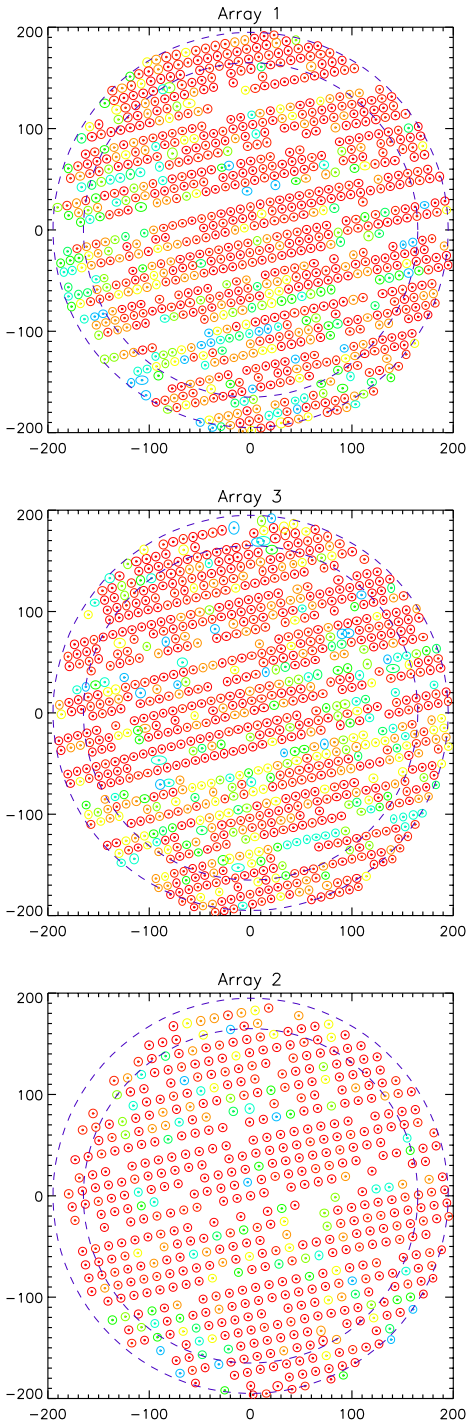


Figure 5: Average detectors positions for arrays A1, A3, and A2 (from green to red as a function of the number of times that a given pixel has been considered as valid). The three plots show the detectors that have seen the sky and passed the quality criteria for at least two beam maps during Run10, 9 and 8: 925, 944, and 543 for A1, A3 and A2, respectively. The inner and outer dash-line circles correspond to a FOV of $5.5'$ and $6.5'$, respectively. Units are arcseconds. The color (from green to red) shows the number of times that a given pixel has been considered as valid.

difference of the mean and median position of each KID (the red crosses and black squares in Fig. 7). For the latter a criteria on the position is applied in order to find the pixels that are closer than the grid step.

5 Pointing accuracy

Based on general operating experience at the 30m telescope, we use the so-called “pointing” or “cross” scans to monitor the pointing during observations. The telescope executes a back and forth scan in azimuth and a back and forth scan in elevation, centered on the observed source. Looking at the timeline profiles of the reference detector, we fit gaussian profiles and derive the current pointing offsets of the system in azimuth and elevation. These offsets can then be passed to PAKO to recenter the next scan (Fig. 8).

Such scans and their analyses are also used to improve the pointing model of NIKA2. A pointing session consists in observing about 30 sources on a wide range of elevations while monitoring the pointing offsets that are measured for each observation. These offsets **and** then passed to the IRAM staff who **then find** the pointing model parameters that minimize and symetrize the scattering of these offsets (cf. Fig. ??). Fig. 9 shows the pointing corrections that had to be applied during Run9, before and after the derivation of the new Nasmyth offsets. While the absolute values of the corrections is somewhat arbitrary and set around zero for convenience, the dispersion of the offsets is the true figure of merit of the pointing corrections. The distribution of corrections after the corrections (in yellow to red) is clearly more symmetric and narrower than before. The pointing accuracy is 1.62 arcsec rms in azimuth and 1.37 arcsec rms in elevation.



6 Beam pattern

The NIKA2 beam pattern mainly depends on the IRAM 30m telescope and NIKA2 internal optical system characteristics, whereas the detectors themselves might have an impact at sub-dominant level (through e.g. time constants or correlated noises). In this section, first we reconstruct the focus surfaces and present the optimal focus, then we characterize both the main beam, which is modeled as an elliptical Gaussian, and the full beam pattern including error beams up to angular scales of 10 arcmin.

6.1 Optimal focus

Owing to the NIKA2 6.5 arcmin FOV, the focus is expected to slightly changes across the FOV, defining curved focal surfaces at the location of the

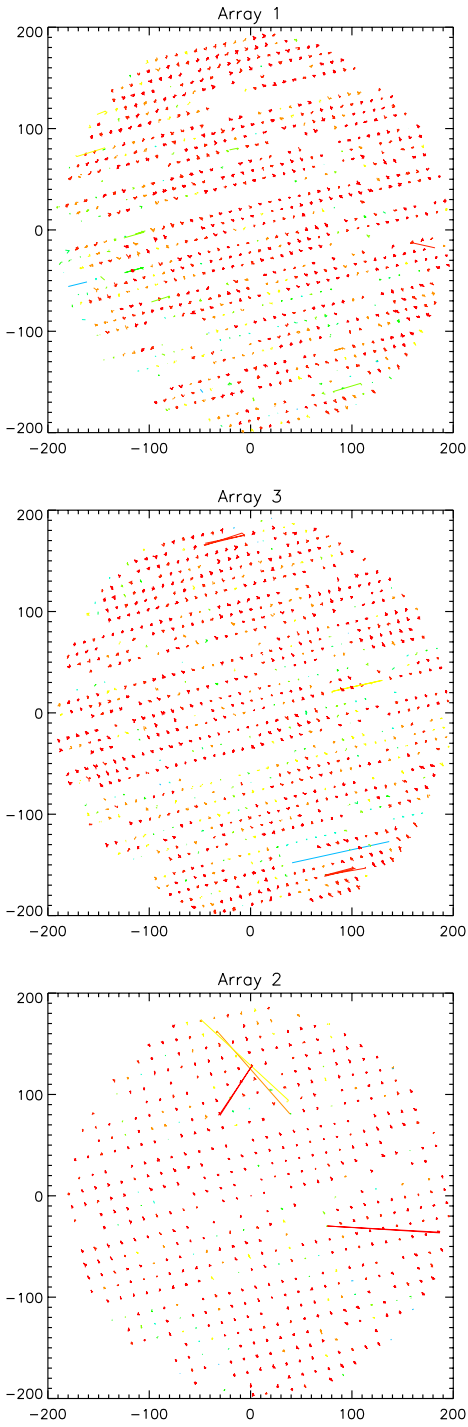


Figure 6: For the 952, 961, and 553 pixels that have passed the quality criteria at least twice for A1, A3 and A2, we show the positions of each pixel, as obtained from each beam map. We can see that some of them are not found at the same position for all the beam maps. Units are arcseconds.

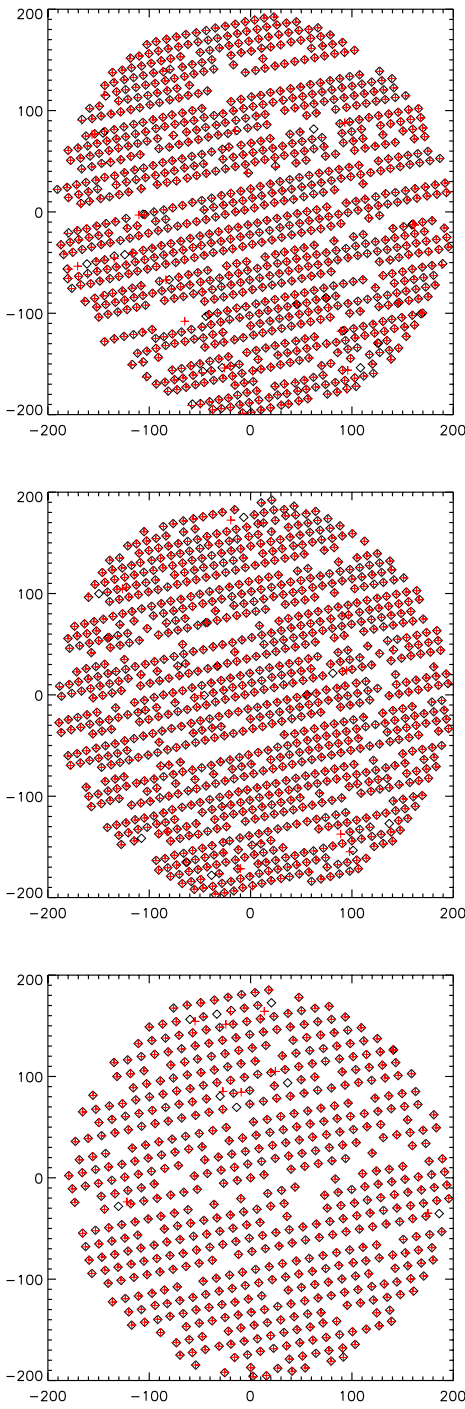


Figure 7: For the 952, 961, and 553 pixels that have passed the quality criteria at least twice for A1, A3 and A2, we show the positions of each pixel, as obtained from each beam map. We can see that some of them are not found at the same position for all the beam maps. Units are arcseconds. The color (from green to red) shows the number of times that a given pixel has been considered as valid. 

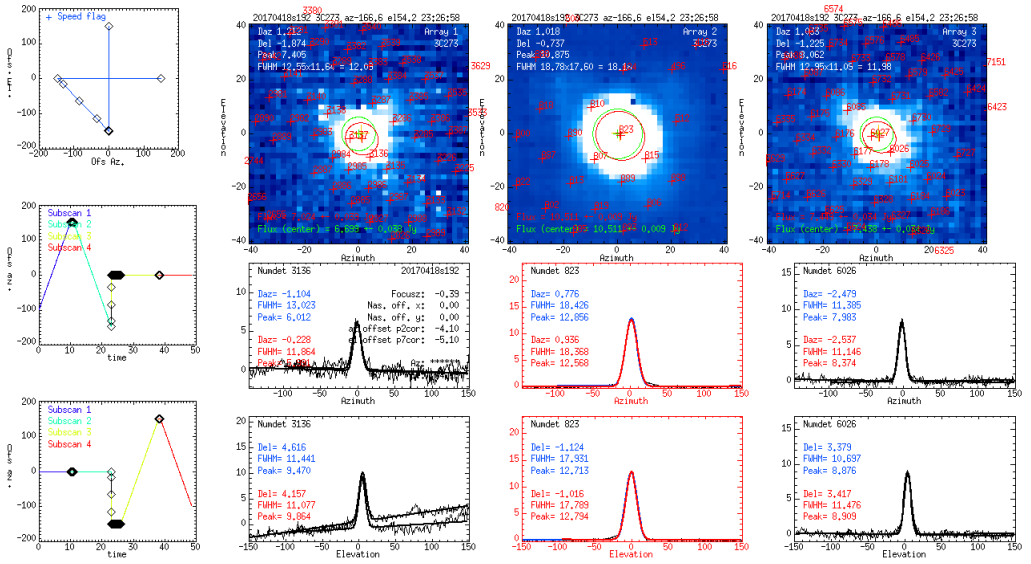


Figure 8: Summary plots of the reduction of pointing scan. There is one combined map per array to check the overall quality of the scan, and a set of azimuth and elevation profiles for one reference detector per array. The 2mm reference detector, highlighted in red, is the the pointing reference detector of NIKA2. The location of the peak in azimuth and elevation, as observed by the reference detector gives the pointing offset of the current scan.

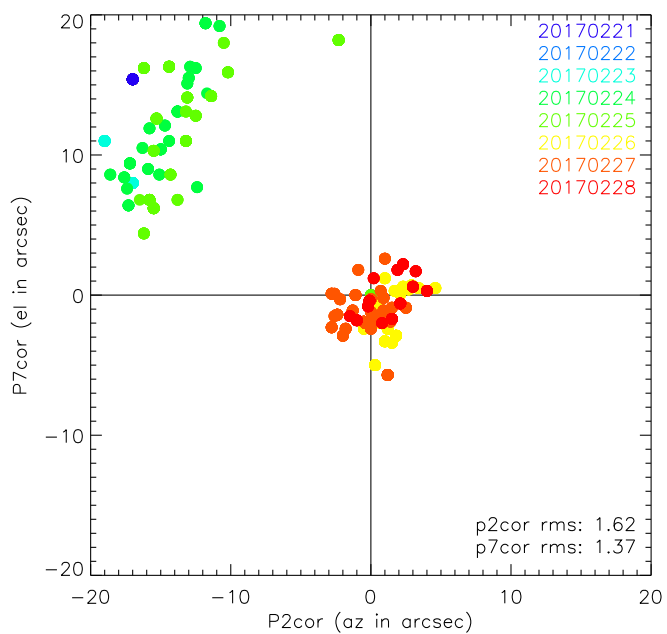


Figure 9: Pointing offsets during Run9 observations, before and after the derivation of Nasmyth offsets with a pointing session on Feb. 26th, 2017.

three arrays. Therefore, beam patterns are expected to show some scatter across the FOV accordingly to the focal surfaces. Although all the detectors cannot be individually focalised, an optimal axial focus of the telescope can be found to maximize the number of detectors at the best focus and hence, maximize the resolution of the NIKA2 maps. This optimal z-focus setting is obtained in measuring the focus at the center of the arrays as described Sect. 6.1.1 and apply a focus shift, which is primary predicted using Zemax simulation, and ultimately verified by measuring the focus surfaces, as described in Sect. 6.1.2.

6.1.1 Focus estimation

The best axial focus in the central region of the arrays is estimated using the so-called 'focus_OTF' PAKO script, which realises a series of five $1' \times 5'$ OTF scans at various values of the focus in 0.4 mm-steps around an *a priori* value z_0 , namely $z \in \{-0.8, -0.4, 0, 0.4, 0.8\} + z_0$. Elliptical Gaussian fit on the reconstructed maps provide estimates of the flux and FWHM along minor- and major-axis for each focus. Then, parabolic fits are used to determine the best focus. We consider three estimates: i) \hat{z}_{peak} the focus that maximizes the estimated flux, which is the amplitude of the 2D Gaussian, ii) \hat{z}_{fwhm} the focus that minimizes the geometrical FWHM, defined as the quadratic mean of $\text{FWHM}_{\text{major}}$ and $\text{FWHM}_{\text{minor}}$, and iii) \hat{z}_{ellipt} the focus that minimizes the beam ellipticity, defined as $\text{FWHM}_{\text{major}}/\text{FWHM}_{\text{minor}}$. Fig. 10 shows an example of axial focus measurement using a 'focus_OTF' observation of Neptune during N2R10.

6.1.2 Reconstruction of the focus surfaces

Method. We measure NIKA2 focal surfaces by means of a sequence of five 'beam-map' scan observations of bright point-like sources, typically Planets or bright quasars, for various settings of the telescope axial focus around the optimal focus z_{opt} . A beam-map scan consists of a deep-integrated $13.5' \times 7.8'$ OTF-scan observation comprising 99 sub-scans and with a scanning speed of $39''/\text{s}$ [TBC]. The z-focus is changed in step of 0.6 mm to probe a large focus range for measuring even the extreme variation of the focus surfaces, namely $z \in \{-1.2, -0.6, 0, 0.6, 1.2\} + z_{\text{opt}}$. Each beam-map scans allow for $4''$ -resolution individual maps per kid to be projected. Before the projection, the correlated noise is mitigated from each KID timeline in subtracting out a common mode, which is obtained using, amongst the other detectors, those that correlates the most with this KID and that are located outside a radius of $90''$ around the source centroid. Therefore, a series of five cleaned maps at various focus is available for each detector, from which

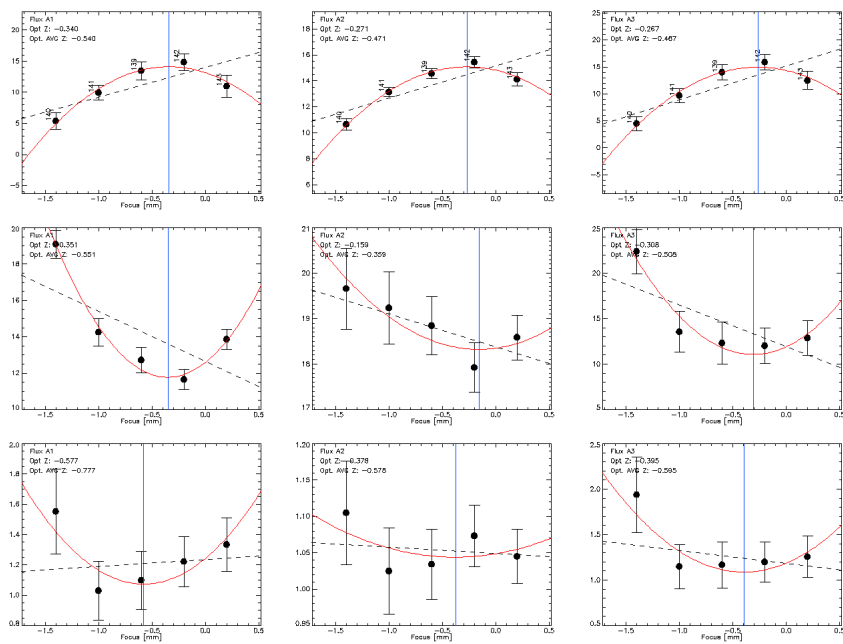


Figure 10: Example of axial focus measurement using a 'focus_OTF' observation of Neptune during N2R10 [PLACEHOLDER]

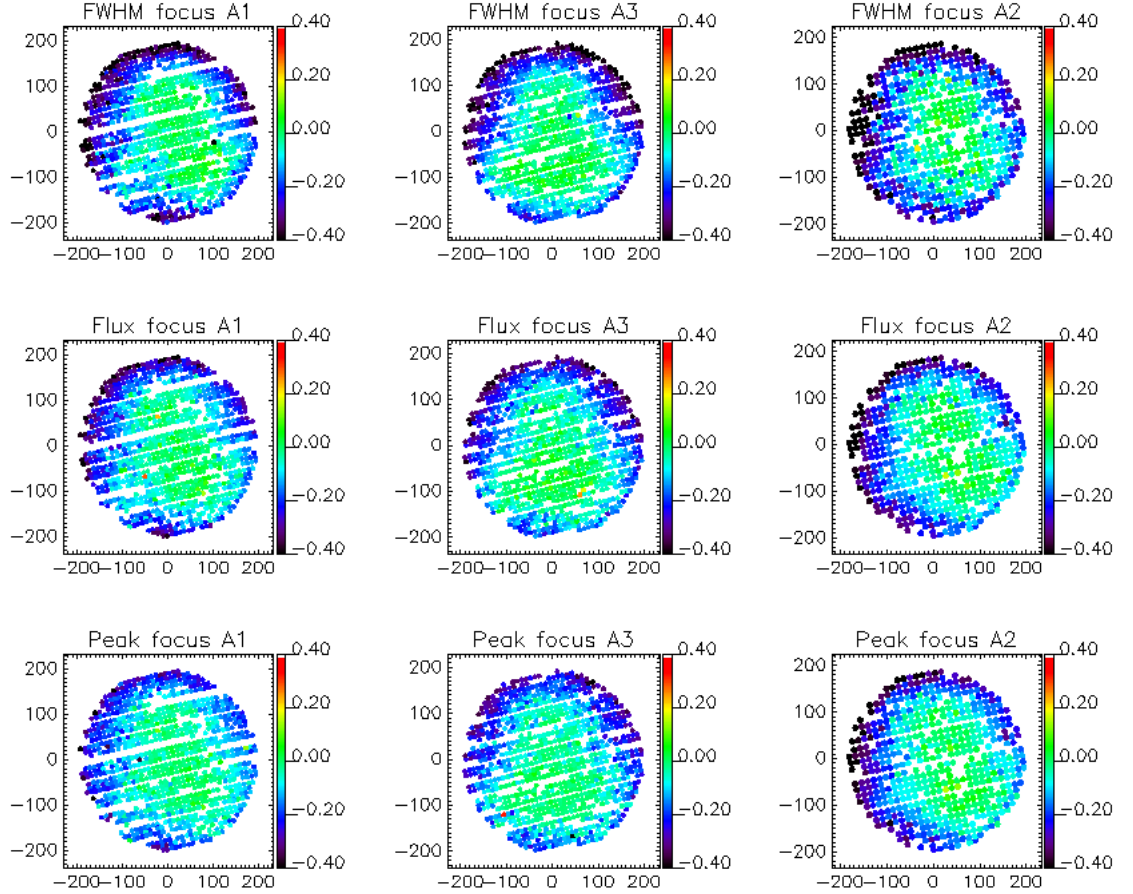


Figure 11: Focus surface of A1, A3 and A2 arrays from left to right. From top to bottom, the focus estimates rely on FWHM-minimization, amplitude-maximization of an elliptical Gaussian of fixed FWHMs and amplitude-maximization of an elliptical Gaussian.

the best focus is estimated as described in Sect. 6.1.1. The ensemble of the relative focus estimate per KIDs with respect to the best focus at the center of the array constitutes the focus surface. An accurate estimate of the center focus is obtained as the weighted average focus estimate of the KIDs lying in a $30''$ radius around the geometrical center of the array. This average does not induce any sizeable bias thanks to the flatness of the focus surface in the innermost regions. For robustness test, we consider three focus estimates: the two first ones are the same as discussed in Sect. 6.1.1 – namely i) \hat{z}_{fwhm} the focus that minimizes the geometrical FWHM and ii) \hat{z}_{peak} the focus that maximizes the amplitude of the best-fitting elliptical Gaussian – whereas the third one is \hat{z}_{flux} the focus that maximizes the amplitude of the best-fitting elliptical Gaussian of fixed FWHM (at $12''$ at 260 GHz and $18''$ at 150 GHz). The comparison between the two amplitude-based estimators (\hat{z}_{peak} and \hat{z}_{flux}), will test the stability of the focus results against the exact choice of the beam fitting function. Since the ellipticity-based estimator \hat{z}_{ellip} is less sensitive to focus changes and yields larger uncertainties than the others, we do not use it for the focus surface reconstruction.

 *Data selection.* During the three commissioning campaigns that occurred after the change of A1 lens (hence in the final NIKA2 optic configuration), nine out-of-focus beam-map scan sequences have been acquired, including incomplete sequences and sequences hindered by poor atmospheric conditions. We select sequences that i) comprises at least four scans, ii) have been observed at zenith opacity at 225 GHz (as indicated by the IRAM taumeter) below 0.5 and iii) have a maximal central focus drift between the starting time and the end of the sequence of 0.5 mm. These criteria preserve five sequences from which focus surfaces can be reconstructed. Namely, we consider the sequences 20170226s415–419, 20170419s133–137, 20170420s113–117, 20170421s160–164 and 20170424s123–127, which consist of observations of the bright quasar '3C84' and Neptune.

Results. For each detector k and each beam-map sequence s , we obtain for the array a , a focus measurement $z_k^{a,s} \pm \sigma_k^{a,s}$, where $\sigma_k^{a,s}$ is the $1-\sigma$ error of the least-square polynomial fit. The focus surface measurements per arrays obtained from the five beam-map sequences are combined using an inverse-variance weighting scheme to obtain the focus surface estimates

$$z_k^{(a)} = \left(\sigma_k^{(a)} \right)^2 \sum_s \frac{z_k^{a,s}}{\left(\sigma_k^{a,s} \right)^2}, \quad (4)$$

with uncertainties

$$\sigma_k^{(a)} = \left[\sum_s \frac{1}{\left(\sigma_k^{a,s} \right)^2} \right]^{-1/2}. \quad (5)$$

We present NIKA2 focus surfaces per arrays obtained as in Eq. 4 in

Fig. 11. The three flavours of focus-estimators provide us with focus surfaces per arrays that are in good agreement with each others and that have a non-axisymmetrical flatten bowl shape consistent with expectations from simulation [TBA, as discussed further below]. The median defocus (that is the relative focus w.r.t. the center) across the detectors is of about -0.1 mm for the three arrays. Maximal defocus values of about -0.6 mm are found for detectors located in the outer top and left regions of the FOV. Finally, a fraction comprised between 20 and 30% of the KIDs has a relative $z \leq -0.2$ mm.

We primarily estimate the uncertainty of the focus surface measurements using the standard deviation between the three estimators $z_k^{(a)}|_{\text{fwhm}}$, $z_k^{(a)}|_{\text{peak}}$ and $z_k^{(a)}|_{\text{flux}}$. We found approximatively homogeneous standard deviation surfaces per arrays, which have median values across the FOV of about 0.03 mm. However, we cross-check this error estimate by forming the quadratic mean of the three inverse-variance error surfaces per arrays, which are defined in Eq. 5 and quoted $\sigma_k^{(a)}|_{\text{fwhm}}$, $\sigma_k^{(a)}|_{\text{peak}}$ and $\sigma_k^{(a)}|_{\text{flux}}$. This provides us with more optimistic error surfaces per array, which do not show any clear pattern across the FOV and which have a median value across the detectors of about 0.015 mm.

[EXPAND THE DISCUSSION ON COMPARISON WITH SIMULATION]

Stability across sequences. By comparing the focus surface obtained from the five individual focus sequences, we test the stability of the NIKA2 focus surfaces across the time and the atmospheric conditions. In Figs. 12-13, we compare the defocus along two perpendicular diameters across the FOV. Although any direction would have been equivalent for this test, we choose to position the diameters along-with and perpendicular-to the KID geometrical grid to avoid the scatter due to KID non-alignement in any other direction. The scatter is further mitigated by considering four-detector-wide diameters as shown in upper the left corner of Figs. 12-13.

[DEVELOP A LITTLE THE DISCUSSION HERE]

6.1.3 Constraints on the X and Y foci

6.2 Full beam pattern

6.2.1 Data sets

The characterization of the IRAM 30-m beam pattern observed through NIKA2 detectors is mainly based on observations of strong compact sources, such as planets including Uranus, Neptune and Mars, and bright quasars. We generally use beam-map scans, which we recall, are deep-integration raster-scan observations that consist of 99 sub-scans placed at intervals

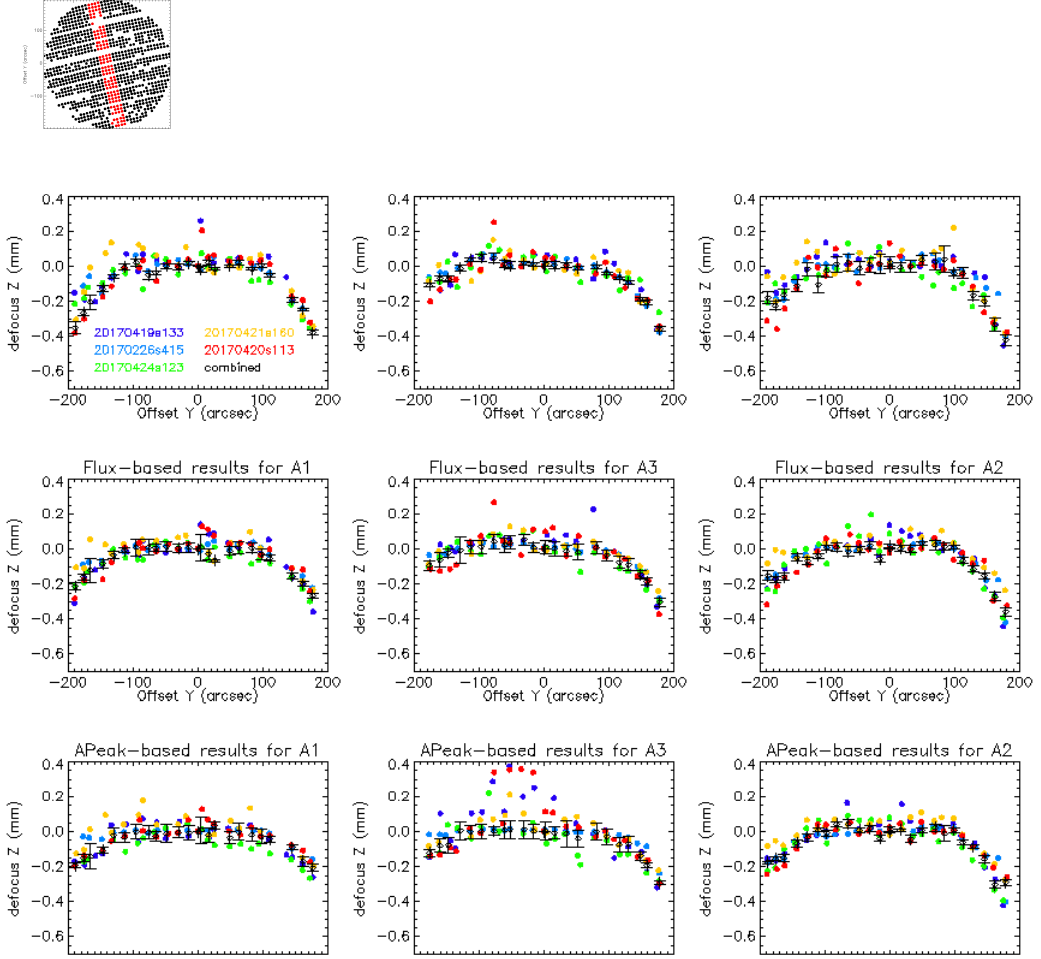


Figure 12: Stability of the focus surface across the sequences. This series of plot show the relative focus with respect to the center (defocus) along the ‘vertical diameter’, that is a band of four-detector width across the FOV, which is vertical with respect to the detector geometrical grid, as illustrated by the plot in the upper left corner. The datapoints show the defocus along the ‘vertical diameter’ estimated from the five focus sequences, namely 20170226s415–419 (sky blue), 20170419s133–137 (dark blue), 20170420s113–117 (red), 20170421s160–164 (yellow) and 20170424s123–127 (green), using the $z^{(a)}|_{\text{fwhm}}$, $z^{(a)}|_{\text{flux}}$ and $z^{(a)}|_{\text{peak}}$ estimators from top to bottom, and for A1, A3 and A2 arrays from left to right. The black datapoints are the five-sequence combined defocus, as presented in Fig. 11, taken along the ‘vertical diameter’, and the errorbars, the five-sequence combined defocus errors along the ‘vertical diameter’.

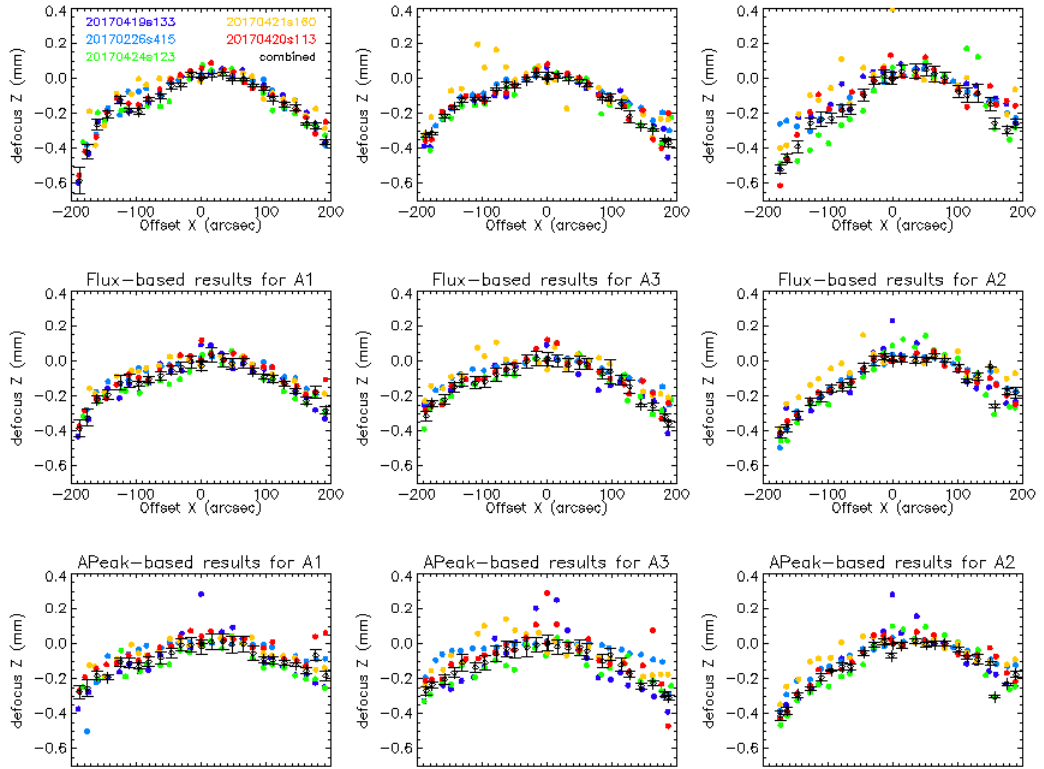


Figure 13: Stability of the focus surface across the sequences. Same legend as in Fig. 12, but for the detectors located in an ‘horizontal diameter’, i.e. a band of four-detector width across the FOV, which is horizontal with respect to the detector geometrical grid, as illustrated by the plot in the upper left corner.

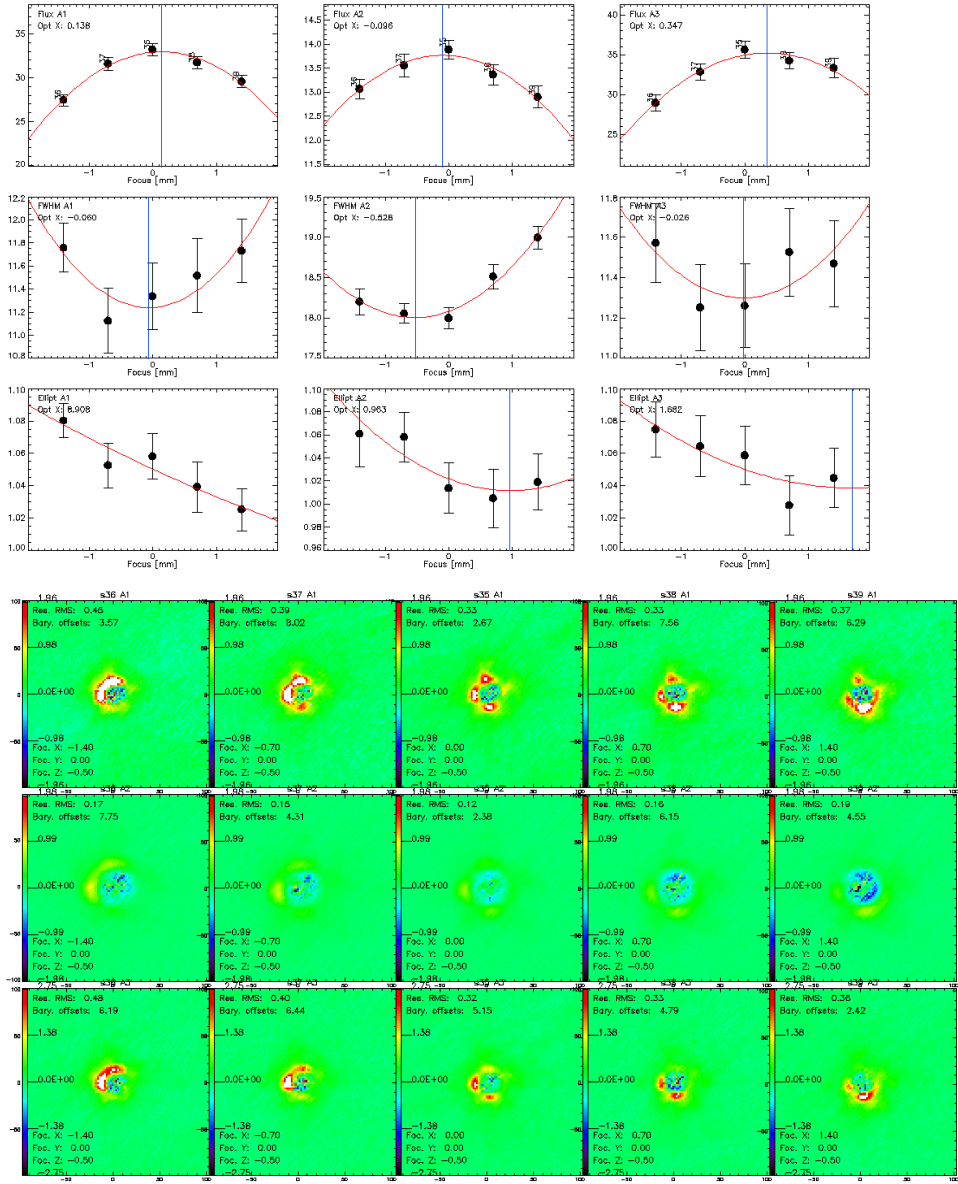


Figure 14: **Left:** X-focus measurement using a parabolic fit of the flux, beam fwhm and ellipticity on a sequence of OTF scans on Uranus. **Right:** Beam residuals after subtracting a model of the main beam for each OTF-scan of the X-focus session.

of $4.8''$ to cover a total of $13.5' \times 7.8'$. Most of our beam-related analysis are based on the same set of beam-map scans as previously selected to perform the average FOV reconstruction. The set comprises nine beam-map scans that distribute as one from N2R8, '20170125s243', two from

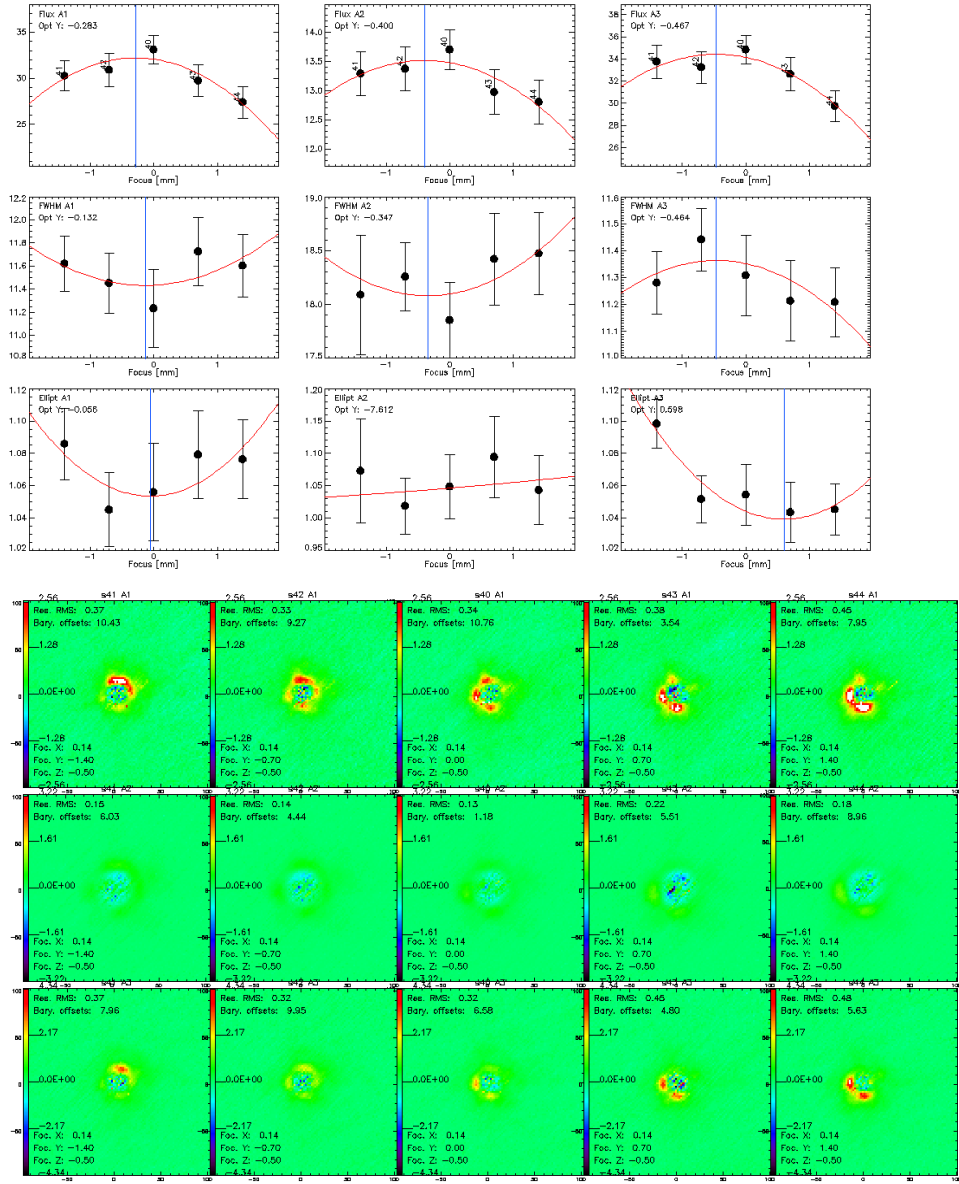


Figure 15: **Left:** Y-focus measurement using a parabolic fit of the flux, beam fwhm and ellipticity on a sequence of OTF scans on Uranus. **Right:** Beam residuals after subtracting a model of the main beam for each OTF-scan of the Y-focus session.

N2R9, '20170224s177' and '20170226s415' and six from N2R10, which are '20170226s425', '20170227s84', '20170419s133', '20170420s113', '20170424s116', '20170424s123'.

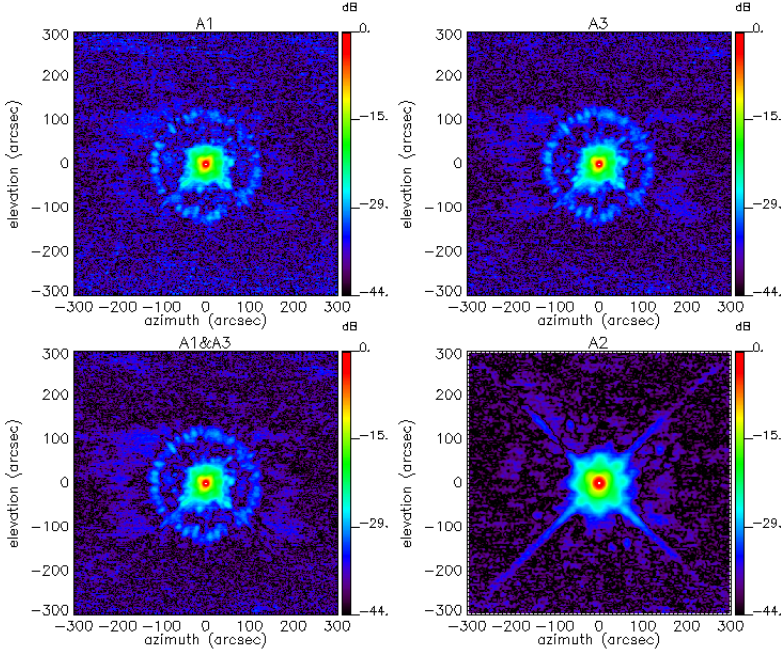


Figure 16: Beam pattern. From upper left to lower right, beam maps of array 1 (labeled 'A1'), array 3 ('A3'), the combination of the 1.15mm arrays ('A1&A3') and the 2mm array ('A2') are shown in decibel. These maps, which consist of normalized combination of four long OTF scans of bright point sources, are in celestial coordinates and cover a sky area which extend over 10 arcmin.

6.2.2 Deep beam maps

We present the two-dimensional distribution of the beam in Fig. 16. We primarily use a map obtained from a combination of deep observations of strong point sources collected during *NIKA2-run8* and *run9*. Namely, we use 'beammap' OTF scans of Uranus (scan id '20170125s223' and '20170125s243'), Neptune ('20170224s177') and the bright quasar 3C84 ('20170226s415'). However, we checked the stability of our results on single scan maps, combinations of scans for a single source, and combinations of shallower scans but spanning a large range of scanning direction. The data processing includes a mitigation of the correlated noise, which mainly originates from the atmosphere. We primarily use a subtraction of a common mode estimated from the most correlated detectors (the so-called 'cm one block' method). However, other methods are tested for assessing the immunity of our results to noise residuals.

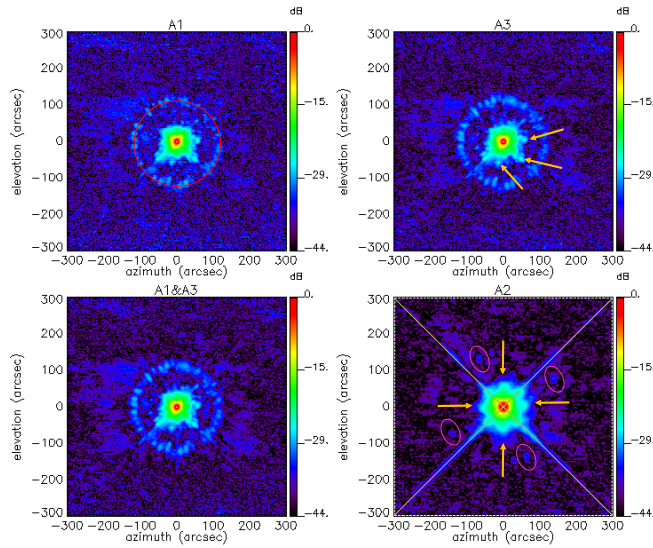


Figure 17: Noticeable features of NIKA2 beam pattern. Red circle: diffraction ring seen in 1-mm maps (the spokes are presumably caused by radial and azimuthal panel buckling (cf. Fig.4 in Greve et al. 2010)); Perpendicular green lines: diffraction pattern caused by quadrupod secondary support structure (prominently seen in 2mm maps); Yellow arrows in the upper right pannel: pattern of 3 spikes seen in 1mm maps of unknown origin; Yellow arrows in the lower right pannel: four symmetrical spokes of the first errorbeam; Pink ellipses: 4 spikes seen in 2mm maps.



The deep NIKA2 beam maps reveal some noticeable features, which are shown in Fig. 17.

To gain a first impression of the structure of the Iram 30-m beam as seen with NIKA2, we use radial cuts to evidence the relative level of the main beam, the first error beam and other features seen in the 2D beam pattern using radial cuts. NIKA2 full beam is shown in Fig. ?? by means of two orthogonal cuts through Uranus from a high quality map obtained on 2017 January 25th in excellent conditions (low opacity $\tau_{225} = 0.08$ and elevation 46°).

A model made of three Gaussians centered on the source peak was best fit *by hand* to these cuts. We observe that the main beam starts to depart from the first Gaussian at the level of about -12dB for the three arrays. We note that for the instrument EMIR on the radiotelescope, this departure is about -20dB (Kramer, Penalver and Greve 2013). The precise characterization of the full beam structure is discussed in Sect. 6.2.3.



6.2.3 Beam profile

6.3 Main beam

We define NIKA2 main beam as the principal Gaussian (of the smaller FWHM) that encloses most of the measured source flux. The principal-power, smaller-FWHM Gaussian fitted function within the three-Gaussian model, as discussed in Sect. 6.2.3, provides us with a first estimate of the main beam, which is given in Table 4. However, this estimate could be biased toward the lower-FWHM values due to degeneracies between the three-Gaussian model parameters. To ensure obtaining robust main beam FWHM estimates, we devise two alternative dedicated methods, which both resort to masking the side lobes: i) Gaussian fits of the beam profile to benefit from the signal-over-noise increase after azimuthally averaging the signal, ii) Elliptical Gaussian fits of the beam map for a better 2D modeling. Cross-checking the outputs from these complementary methods is an important robustness test of our results.

We also consider different data sets acquired during *N2R8*, *N2R9* and *N2R10*: i) a series of $8' \times 5'$ OTF scans of primary and secondary calibrators, ii) beam-map scans of Planets.

Table 4 gathers the main beam FWHM results obtained using the three discussed methods and two datasets. 

6.3.1 Sidelobe-masked Profile-based analysis

[JEAN-FRANCOIS]

6.3.2 Sidelobe-masked Map-based analysis

Method description NIKA2 main beam two-dimensionnal distribution is modeled using an elliptical Gaussian. We characterize NIKA2 resolution by giving the *FWHM*, defined as

$$FWHM = 2\sqrt{2 \ln 2} \sqrt{\sigma_x \sigma_y}, \quad (6)$$

where σ_x and σ_y are the Gaussian standard deviation along minor- and major-axis. To avoid the side lobes contamination, we use masked versions of the beam map, in which an annulus of inner radius r_{in} and outer radius r_{out} is cut out. Whereas r_{out} is conservately set to be 100arcsec , r_{in} is let free to vary around a central value about $8'$ for A1 and A3 and about $12'$ for A2 to provide the best 2D Gaussian fit.

Estimates using $8' \times 5'$ OTF scans We select *N2R9* and *N2R10* $8' \times 5'$ OTF scans of bright point sources, including primary and secondary calibrators.

Namely, we consider scans of Uranus, Neptune, 3C273, 3C84, 0316+413, Vesta and MWC349, whereas we avoid CRL2688 and NGC7027, which are slightly extended. Conservative data selection criteria with respect to observing conditions are applied: average elevations $\text{el} \geq 20$, zenith opacities as estimated by NIKA2 in the 1mm band $\tau_{1\text{mm}} \leq 0.4$, reasonable lateral focus settings $x, y \leq 0.5\text{mm}$. After selection cuts, our data set includes 130 OTF scans acquired during *N2R9*, which consists of a representative sub-sample of a typical NIKA2 observation campaign, as well as **XXX** scans of *N2R10*.

Figure 20 shows FWHM distributions obtained **in** using the elliptical Gaussian fit method from the selected set of $8' \times 5'$ OTF scans. We checked a posteriori that r_{in} distributes as $7 \pm 1.5 \text{ arcsec}$ at 1mm and $13 \pm 4 \text{ arcsec}$ at 2mm, in agreement with settings defined in the profile-based analysis.

Estimates using beam-map scans The elliptical Gaussian model **is best** fit to sidelobe-masked beam-maps from the scan selection described in Sect. 6.2.1. Sidelobe masks are defined by a fixed r_{out} of 100arcsec and a r_{in} that freely varies from $8'$ to $9'$ for the 260 GHz-arrays, and from $10'$ to $14'$ for the 150 GHz array. We checked, however, that we obtain consistent results but larger dispersion when using annulus masks of fixed r_{in} of $8.5'$ and $12'$ at 260 and 150 GHz respectively. The median main beam FWHM and the rms error estimate, **as** obtained from the nine beam-maps, are given in Table 4.

Table 4: FWHM of the NIKA2 main beam in arcsec.

Array	A1	A3	A1 & A3	A2
Three-Gaussian model G1 ^a	10.8 ± 0.2	10.8 ± 0.2	10.8 ± 0.3	17.2 ± 0.05
Sidelobe-masked profile-based				
Sidelobe-masked map-based OTF	11.0 ± 0.3	10.9 ± 0.2	11.0 ± 0.2	17.8 ± 0.2
Sidelobe-masked map-based beam-map				

^(a) Median FWHM of the first (lowest-FWHM) Gaussian function within the Three-Gaussian model fitted from the beam-map scan selection

6.4 Beam efficiency

6.5 Stability of the beam pattern

[A FAIRE:

AJOUTER LES PLOTS DE STABILITE EN FONCTION DE ELEVATION,

TAU

J

7 Calibration

The calibration of the instrument NIKA2 in its final configuration of January 24th 2017 is studied in this section in using the primary calibrators, Uranus and Neptune, and secondary calibrators ; the two largest asteroids Ceres and Vesta, and the three planetary nebulae NGC7027, CRL2688, and MWC349.

Agaga

7.1 NIKA2 Photometric System

	1mm	2mm
Reference frequency ν_0	260 GHz	150 GHz
Reference FWHM	12.5 "	18.5 "

Table 5: NIKA2 reference frequencies and FWHM

7.1.1 Response of a detector to astronomical source

Let us consider a source observed at airmass $\sec z$ under mm_{H_2O} of precipitable water, with specific intensity I_ν (in units of $W/m^2/sr/Hz$) in the direction θ, ϕ , where θ is the off-axis distance and ϕ the position angle, illuminating a KID of the NIKA2 array.

A KID response located at position θ, ϕ on the focal plane to this signal will be:

$$R(\theta, \phi, \sec z, mm_{H_2O}) = G_k \int_0^{+\infty} I(\nu) \frac{T'(\nu)}{\left(\frac{\nu}{\nu_0}\right)^2} e^{-\sec z \cdot \tau(\nu, mm_{H_2O})} A\Omega(\nu) d\nu \quad (7)$$

where the different factors in the integral are:

- $\frac{T'(\nu)}{\left(\frac{\nu}{\nu_0}\right)^2}$: the system transmission. $T'(\nu)$ is the transmission as measured in section 2 with a Rayleigh-Jeans source. It is divided by $\left(\frac{\nu}{\nu_0}\right)^2$ to correct for the incident spectrum.
- $e^{-\sec z \cdot \tau(\nu, mm_{H_2O})}$: the atmospheric transmission at airmass $\sec z$ for an amount of precipitable water vapor mm_{H_2O} generating an opacity $\tau(\nu)$.
- $A\Omega(\nu)$: the KID etendue, *i. e.* the product of its light collecting area by the solid angle it intercept on the sky. While the step between pixels is well known and is measured (see sec 4.1), the actual solid angle is not

known precisely and is *probably* a function of the frequency because the pixels sizes are close to the wavelength of operation (2.75 mm at 2mm for example). The collecting **A** area is the projection of the IRAM primary on the cold pupil and is also not known very accurately. 

The integral in eq 7 gives the total power (units of W) falling on a pixel. The factor G_k (units of W^{-1}) convert this power to ADU. 

By virtue of the conservation of specific intensity in a telescope, equation 7 can be rewritten as:

$$R(\theta, \phi, \sec z, mm_{H_2O}) = G_k A_p \Omega_s \int_0^{+\infty} I(\nu) \frac{T'(\nu)}{\left(\frac{\nu}{\nu_0}\right)^2} e^{(-\sec z \cdot \tau(\nu, mm_{H_2O}))} \Omega_b(\theta, \phi, \nu) d\nu \quad (8)$$

where:

- A_p is the area of the entrance pupil (*i.e.* the dish collecting area).
- Ω_s is the solid angle of the source seen from the entrance pupil.
- $\Omega_b(\theta, \phi, \nu)$ is the fraction of source signal illuminating the KID. It is thus normalized so that:

$$\int \int_{4\pi} \Omega_b(\theta, \phi, \nu) \sin \theta d\theta d\phi = 1 \quad (9)$$

Equation 8 describes the response of a KID, and it is quite complex. We will in the following simplify it by making a few assumptions. Let us first turn ourselves toward the effect of the atmosphere. 

7.1.2 Effect of the atmosphere

In order to study the effects of the atmosphere, let us define the effective frequency of a source as the weighted frequency of the passband, taking into account the system and atmospheric transmission, as well as the shape of the incident spectrum:

$$\nu_{eff}(\sec z, mm_{H_2O}) = \frac{\int_0^{+\infty} I(\nu) \frac{T'(\nu)}{\left(\frac{\nu}{\nu_0}\right)^2} e^{(-\sec z \cdot \tau(\nu, mm_{H_2O}))} \nu d\nu}{\int_0^{+\infty} I(\nu) \frac{T'(\nu)}{\left(\frac{\nu}{\nu_0}\right)^2} e^{(-\sec z \cdot \tau(\nu, mm_{H_2O}))} d\nu} \quad (10)$$

In order to compute the atmospheric transmission, we have used the IRAM atmosphere 2009 models provided in GILDAS, computed for 'midlatwinter' conditions, a temperature of 268 K and a pressure of 703.5 hPa. ν_{eff} allows to characterise the impact of the variation of the atmospheric transmission

on the full system transmission. Note that the instrument transmission $T'(\nu)$ is the one measured in sec 2.

Figure 21 shows the variations of ν_{eff} as a function of the water content of the atmosphere for two elevations (zenith and 20 degree) and two spectral shape (RJ and flat spectrum), in the two 1mm passbands and in the 2mm passband.

Typical variations of ν_{eff} with the spectral shape of the source range between 1% and 3%, and are relatively stable between good ($\tau_{225GHz} \simeq 0.1$) and poor ($\tau_{225GHz} \simeq 1.0$) atmospheric conditions for both the 1mm and 2mm bands.

Let us now examine the effect of elevation. Under good atmospheric conditions ($\tau_{225GHz} \simeq 0.1$), ν_{eff} change by less than 0.3% between zenith and 20 degree elevation. Under poor conditions ($\tau_{225GHz} \simeq 1.0$), this rises to almost 3% for a Rayleigh-Jeans spectrum in the 2mm band, *i.e.* larger than the variations due to the spectral shape of the source.

Nevertheless, to a first approximation, we consider the shape of the atmospheric transmission independent of the elevation and water content, so that an effective zenith opacity τ_{eff} used. Equation 8 becomes under this assumption:

$$R(\theta, \phi, \sec z, mm_{H_2O}) \simeq G_k A_p \Omega_s e^{(-\sec z \cdot \tau_{eff}(mm_{H_2O}))} \int_0^{+\infty} I(\nu) \frac{T'(\nu)}{\left(\frac{\nu}{\nu_0}\right)^2} T_{atm}(\nu) \Omega_b(\theta, \phi, \nu) d\nu \quad (11)$$

where $T_{atm}(\nu)$ is the transmission of the atmosphere at zenith, and is a function of the frequency only. From the computations made to plot figure 21, we derive that this approximation is valid below the percent level for $\tau_{225GHz} < 0.35$

The dependence on elevation and opacity can be corrected as shown in section 3, so that a response outside of atmosphere (in terms of airmass, but not in terms of transmission) can be derived:

$$R(\theta, \phi) \simeq G_k A_p \Omega_s \int_0^{+\infty} I(\nu) \frac{T'(\nu)}{\left(\frac{\nu}{\nu_0}\right)^2} T_{atm}(\nu) \Omega_b(\theta, \phi, \nu) d\nu \quad (12)$$

Equation 12 is the main photometric equation.

Because both A_p and Ω_b are not known with good accuracy, it is not possible to compute all the terms of eq. 12 from first principles, and a practical way of calibrating the system must be used: it is done by observing a primary calibrator.

7.1.3 Beammapping of a calibrator

A primary calibrator is a source whose spectral irradiance is known. For NIKA2, we use two planets as primary calibrators, Uranus and Neptune.

The specific intensity $I_c(\nu)$ of the calibrator is:

$$I_c(\nu) = \frac{S_c(\nu)}{\Omega_s} = \frac{S_c(\nu_0)}{\Omega_S} f\left(\frac{\nu}{\nu_0}\right) \quad (13)$$

Where $S_c(\nu)$ is the spectral irradiance of the calibrator (units of $W/m^2/Hz$) or Jy. We parametrize the source spectral irradiance as a function of a reference frequency ν_0 that we choose arbitrarily to be: $\nu_0 = 150$ GHz for the 2mm array and $\nu_0 = 260$ GHz for both 1mm arrays.

Equation 12 becomes:

$$R(\theta, \phi) \simeq G_k A_p S_c(\nu_0) \int_0^{+\infty} f\left(\frac{\nu}{\nu_0}\right) \frac{T'(\nu)}{\left(\frac{\nu}{\nu_0}\right)^2} T_{atm}(\nu) \Omega_b(\theta, \phi, \nu) d\nu \quad (14)$$

Let further parametrize the beam as a function of the effective frequency as defined in eq 10, considering that its frequency dependency is only due to the **diffraction** law, hence a variation as $1/\nu$.

With this in hand, we can write the equation of a beammapping using a single KID with eq 11. At each position (θ, ϕ) on the beam map we have:

$$R_c(\theta, \phi) = G_k A_p S_c(\nu_0) \int_0^{+\infty} f\left(\frac{\nu}{\nu_0}\right) \Omega_b\left(\nu_0, \theta \times \frac{\nu}{\nu_0}, \phi\right) \frac{T'(\nu)}{\left(\frac{\nu}{\nu_0}\right)^2} T_{atm}(\nu) d\nu \quad (15)$$

7.1.4 Calibration in $FWHM_0$ beam

This map is fitted with **au** gaussian of fixed width: $FWHM_0$ (we recall that $2\sqrt{2 \ln 2} \sigma_0 = FWHM_0$). 

$$R_c(\theta, \phi) = \frac{A_c}{2\pi\sigma_o^2} e^{-\frac{\theta^2}{2\sigma_o^2}} + \epsilon(\theta, \phi) \quad (16)$$

where $\epsilon(\theta, \phi)$ are the residuals of the fit.

Assuming that the fit is not biased, we have:

$$\int \int R_c(\theta, \phi) \sin \theta d\theta d\phi = A_c \quad (17)$$

because errors average out so that:

$$\int \int \epsilon(\theta, \phi) \sin \theta d\theta d\phi = 0 \quad (18)$$

But we also know that integral of the beammap should give the power emitted by the source. Therefore we form the map:

$$M_c(\theta, \phi) = R_c(\theta, \phi) S_c(\nu_0) / A_c \quad (19)$$

 Where $S_c(\nu_0)$ is the spectral irradiance of the calibrator at a reference frequency ν_0 given in table 7.1. This map has units of $W/m^2/Hz$. Note that the choice of the reference frequency is arbitrary, it is a convention. By construction, integrating over the map we have:

$$\int \int M_c(\theta, \phi) \sin \theta d\theta d\phi = S_c(\nu_0) \quad (20)$$

Similarly, a point source with spectral irradiance $S_s(\nu)$ will generate a response at position (θ, ϕ)

$$R_s(\theta, \phi) = G_k A_p \int_0^{+\infty} S_s(\nu) \Omega_b(\nu_0, \theta \times \frac{\nu}{\nu_0}, \phi) \frac{T'(\nu)}{\left(\frac{\nu}{\nu_0}\right)^2} T_{atm}(\nu) d\nu \quad (21)$$

Note here that the effective frequency for the beam is not necessarily the same as the one for the primary calibrator, as it depends on the source spectrum.

This beammap will be fitted with a gaussian of fixed width:

$$R_s(\theta, \phi) = \frac{A_s}{2\pi\sigma_0^2} e^{-\frac{\theta^2}{2\sigma_0^2}} + \epsilon(\theta, \phi) \quad (22)$$

The quoted flux for the source is then:

$$S_q(\nu_0) = S_c(\nu_0) \times \frac{A_s}{A_c} \quad (23)$$

In other words, the quoted flux is the flux that should have the calibrator in order to generate a response that would be fitted with a gaussian of fixed width and the same amplitude as the source. Let us form the map:

$$M_s(\theta, \phi) = R_s(\theta, \phi) S_c(\nu_0) / A_c \quad (24)$$

The map $M_{\theta, \phi}$ is said to be calibrated in Jy / FWHM₀ beam.

If we have a single point source in M,  we have when we fit a gaussian of fixed width:

$$\int \int M_s(\theta, \phi) \sin \theta d\theta d\phi = A_s S_c(\nu_0) / A_c = S_q(\nu_0) \quad (25)$$

Note that the quoted flux is *not* the flux of the source at the reference frequency. In order to find the flux of the source at the reference frequency, a color correction has to be applied

$$S_s(\nu_0) = S_q(\nu_0) C_s \quad (26)$$

7.1.5 Color correction for point sources measured with fixed gaussian fit

When a source is measured

$$C_s = S_s(\nu_0)/S_q(\nu_0) = S_s(\nu_0)/S_c(\nu_0) \times \frac{A_c}{A_s} \quad (27)$$

$$C_s = S_s(\nu_0)/S_c(\nu_0) \times \frac{\int \int R_c(\theta, \phi) \sin \theta d\theta d\phi}{\int \int R_s(\theta, \phi) \sin \theta d\theta d\phi} \quad (28)$$

$$C_s = S_s(\nu_0)/S_c(\nu_0) \times \frac{\int \int G_k A_p S_c(\nu_0) \int_0^{+\infty} f(\frac{\nu}{\nu_0}) \Omega_b(\nu_0, \theta \times \frac{\nu}{\nu_0}, \phi) \frac{T'(\nu)}{\left(\frac{\nu}{\nu_0}\right)^2} T_{atm}(\nu) d\nu \sin \theta d\theta d\phi}{\int \int G_k A_p \int_0^{+\infty} S_s(\nu) \Omega_b(\nu_0, \theta \times \frac{\nu}{\nu_0}, \phi) \frac{T'(\nu)}{\left(\frac{\nu}{\nu_0}\right)^2} T_{atm}(\nu) d\nu \sin \theta d\theta d\phi} \quad (29)$$

which simplifies into:

$$C_s = S_s(\nu_0) \times \frac{\int_0^{+\infty} f(\frac{\nu}{\nu_0}) \int \int \Omega_b(\nu_0, \theta \times \frac{\nu}{\nu_0}, \phi) \sin \theta d\theta d\phi \frac{T'(\nu)}{\left(\frac{\nu}{\nu_0}\right)^2} T_{atm}(\nu) d\nu}{\int_0^{+\infty} S_s(\nu) \int \int \Omega_b(\nu_0, \theta \times \frac{\nu}{\nu_0}, \phi) \sin \theta d\theta d\phi \frac{T'(\nu)}{\left(\frac{\nu}{\nu_0}\right)^2} T_{atm}(\nu) d\nu} \quad (30)$$

We have:

$$\int \int \Omega_b(\nu_0, \theta \times \frac{\nu}{\nu_0}, \phi) \sin \theta d\theta d\phi = 1 \quad (31)$$

So that:

$$C_s = S_s(\nu_0) \times \frac{\int_0^{+\infty} f(\frac{\nu}{\nu_0}) \frac{T'(\nu)}{\left(\frac{\nu}{\nu_0}\right)^2} T_{atm}(\nu) d\nu}{\int_0^{+\infty} S_s(\nu) \frac{T'(\nu)}{\left(\frac{\nu}{\nu_0}\right)^2} T_{atm}(\nu) d\nu} \quad (32)$$

7.1.6 Calibration for aperture photometry

For aperture photometry, the map calibrated in Jy / $FWHM_0$ must be converted in a map in Jy / pixel.

7.1.7 Calibration in surface brightness

7.2 Reference flux densities of the calibrators

The two main calibrators of NIKA2 are the giant planets Uranus and Neptune. Mars can also be used as primary calibrator, but care must be taken to use a flux corresponding to the date of the observations. Secondary calibrators were also observed during the commissioning campaign.

	Uranus	Neptune
r_e [km]	25559	24764
r_p [km]	24973	24341
ϕ	Ob-lat	Ob-lat
D [AU]	delta	delta

Table 6: Physical quantities used for the Uranus and Neptune fluxes computation (equation 34). Ob-lat and delta are quantities tabulated by NASA Horizons system as a function of the date

7.2.1 Uranus and Neptune

For the flux densities of Neptune we use the ESA model Version 5 from available <https://www.cosmos.esa.int/web/herschel/calibrator-models>. For Uranus, we use the ESA model Version 4 available from the same source. Both models provide the planet brightness temperature in the Rayleigh-Jeans approximation as a function of the frequency. The resulting flux is therefore:

$$S_\nu = \Omega \times \frac{2\nu^2 k T_{RJ}}{c^2} \quad (33)$$

where Ω is the solid angle of the planet on the sky. Following Bendo et al. (2013) and correcting their equation 12 we have:

$$\Omega = \pi \frac{r_e r_{p-a}}{D^2} \quad (34)$$

where r_e is the equatorial radius of the planet and r_{p-a} is its apparent polar radius, and D the distance to the planet. r_{p-a} can be computed from the sub-observer latitude ϕ (e.g. the latitude of the observed as seen from the planet in the planet equatorial reference frame) and r_p the polar radius of the planet as:

$$r_{p-a} = \sqrt{r_p^2 \cos^2 \phi + r_e^2 \sin^2 \phi} \quad (35)$$

All quantities to compute the planet flux are obtained from the NASA Horizons web site <https://ssd.jpl.nasa.gov/horizons.cgi>, and are listed in table 6

To compute the planet fluxes for a given date, we use the python photometry package available at <https://github.com/hausse1/photometry>.

The model spectra are linearly interpolated in log space at the reference frequencies of the NIKA2 bandpasses. Fluxes for all NIKA2 calibration runs are listed in table 7.5, together with the expected variation between the start and end of a run.

The Uranus and Neptune models have been compared to Planck observations of these planets (Planck intermediate results LII, Planck Collaboration in press). For Uranus, the model used in the comparison is the ESA V2, and it is found to overpredict by 4K (about 4%) the observed RJ temperature at 143 GHz and to agree at 217 GHz, and underpredict at 353 GHz. We use for NIKA2 calibration ESA model V4, that predict a flux respectively -3.3%, 0.3% and 4.7% higher in the the 143, 217 and 353 GHz, that would lead to a percent accuracy with respect to Planck observations.

For Neptune, the same study compared Planck observation with the ESA V5 model, *i. e.* the same one used for NIKA2 calibration. For this planet, temperatures are found to disagree at most by 5K, i.e 4.1%, with the same trend with frequency as observed for Uranus. All thing considered, this study confirm that Uranus ESA V4 and Neptune ESA V5 models are accurate to 5% for predicting planet fluxes. Calibration values tabulated in table ?? show that the variations of Uranus and Neptune over the duration of a typical NIKA2 run are negligible compared to the model accuracy. On the other hand, not taking into account the planet shape and orientation with respect to the observer in the computations of its solid angle can lead to errors between 1 and 2% as illustrated in the Python notebook https://github.com/haussel/photometry/blob/master/notebooks/planet_fluxes.ipynb distributed with the software.

7.2.2 Mars

For Mars, we use the model of Belloche & Amri (2006) available at <http://www.lesia.obspm.fr/perso/emmanuel-lelloouch/mars/index.php>, with default parameters. Model output is computed at the two reference frequencies of NIKA2, 150 and 260 GHz.

Fluxes of Mars are tabulated in table 7.5. In many cases, the variations of Mars flux during the course of a run are larger than the model uncertainty (5%), and should be recomputed at more frequent times.

7.2.3 Secondary calibrators: asteroids

The asteroids Ceres and Vesta have been modeled by Muller et al (2014) in accounting for size, shape, spin-properties, albedo, and thermal properties and in adjusting to PACS, SPIRE and HIFI observations of Herschel with an accuracy of 5%. Thomas Mueller has tabulated flux densities at different wavelengths, in particular at $1300\mu\text{m}$, every five days until 2020¹. We have used the prediction at $1300\mu\text{m}$ made for 23rd february 2017 and extrapolated it to the central frequencies of the arrays in using a Rayleigh-Jeans spectrum

¹<http://www.iram.es/IRAMES/mainWiki/Continuum/Calibrators>

NR ^a	JD ^b	Δt ^c	$S_\nu(260 \text{ GHz})$ ^d	$S_\nu(150 \text{ GHz})$ ^e	$\Delta S_\nu / S_\nu^f$
	d	d	Jy	Jy	%
Uranus					
13	2457330.5	12	45.59	17.65	-0.89
14	2457354.5	8	44.44	17.21	-1.07
15	2457409.5	20	40.62	15.73	-3.22
16	2457455.5	14	38.27	14.82	-1.16
18	2457660.0	25	46.06	17.83	+1.25
19	2457690.0	7	46.09	17.85	-0.32
20	2457732.0	7	44.14	17.09	-1.04
21	2457764.5	4	41.82	16.19	-0.69
22	2457809.0	7	39.08	15.13	-0.83
23	2457865.0	7	37.96	14.70	+0.14
24	2457915.4	5	39.49	15.29	+0.66
Neptune					
13	2457330.5	12	17.09	7.18	-1.26
14	2457354.5	8	16.64	6.99	-0.92
15	2457409.5	20	15.76	6.62	-1.35
16	2457455.5	14	15.55	6.53	+0.19
18	2457660.0	25	17.65	7.41	-1.30
19	2457690.0	7	17.24	7.24	-0.68
20	2457732.0	7	16.46	6.91	-0.79
21	2457764.5	4	15.92	6.68	-0.34
22	2457809.0	7	15.56	6.53	-0.08
23	2457865.0	7	15.89	6.67	+0.57
24	2457915.4	5	16.73	7.02	+0.56
Mars					
13	2457330.5	12	146.19	48.30	+7.75
14	2457354.5	8	175.88	58.14	+8.70
15	2457409.5	20	319.71	105.62	+27.68
16	2457455.5	14	666.46	218.49	+30.37
18	2457660.0	25	597.17	199.44	-21.61
19	2457690.0	7	439.23	146.24	-4.82
20	2457732.0	7	311.78	103.98	-4.89
21	2457764.5	4	239.37	79.54	-2.12
22	2457809.0	7	174.99	57.94	-4.94
23	2457865.0	7	123.61	40.61	-5.44
24	2457915.4	5	102.08	33.68	+0.59

Table 7: NIKA2 Planet fluxes. a: Nika Run, b: Julian Date when the model are computed, c: Run duration, d, e: total fluxes at 260 and 150 GHz, f: variation of the 150 GHz flux density over the duration of the run

expected for Ceres and Vesta. Their flux densities in Table 7.5 are for this date. Over the five days of run 9 (february 23 - 28), the flux densities at $1300\mu\text{m}$ have decreased by 3% for Ceres and by 6% for Vesta in Muller's tables but we have not corrected for this effect in our analysis below.

The secondary calibrator MWC349A is a young Be star, part of a stellar binary system, surrounded by a disk. Its radio continuum emission originates in an ionized bipolar outflow (Tafoya et al 2004). MWC349 has been monitored with the Plateau de Bure interferometer and shown to be only slightly angularly resolved, making it a point source for the 30-metre telescope. We have adopted its flux densities from this monitoring². The secondary calibrator CRL2688 is an Asymptotic Giant Branch star. Its radio continuum emission is mostly from circumstellar dust and is somewhat extended (Knapp et al 1994). Its flux densities at $850\mu\text{m}$ and $450\mu\text{m}$ have been stable at the 5% level as monitored by SCUBA2 (Dempsey et al 2013). We have extrapolated their flux densities to the central frequencies of the arrays with a power law of index $\alpha = -2.47$ derived from these SCUBA2 measurements. The secondary calibrator NGC7027 is a young, dusty, carbon rich Planetary Nebula with an ionized core. It is extended in the continuum and molecular lines (Bieging et al 1991) and is not a point source for the telescope. Its most recent flux densities are reported at $1100\mu\text{m}$ and $2000\mu\text{m}$ by Hoare et al (1992). It has been reported to decrease by ~ 0.145 percent/yr in the optically thin part of its spectrum above 6 GHz from VLA observations (Zijlstra, van Hoof & Perley 2008, and Hafez et al, 2008) that makes these flux densities uncertain by 3.6% at present. Its SED from cm wavelengths to optical is also presented in Hafez, Y.A. et al (2008). The flux densities adopted at the central frequencies of the arrays for these three calibrators are in Table 7.5.

7.3 Aperture photometry

The calibrators were observed frequently during runs 9 and 10. These observations were beammmaps for Uranus and Neptune as well as sequences of 4 consecutive off maps ($8' \times 5'$) as done for Ceres, Vesta, NGC7027, CRL2688, and MWC349. All observations were processed to produce intensity maps for the three arrays with the pipeline `in` using `kidpar`, `kidpar-best3files-FXDC0C1-GaussPhot` for the array geometry, the method COMMON-MODE-ONE-BLOCK to remove low frequency noise including atmosphere, sky projection AZEL, line-of-sight opacities, an *a priori* mask of $100''$ and no iteration in mapping. Note that the gain variation with elevation from EMIR implemented in the pipeline has not been used. In addition to the fact



²<http://www.iram.fr/IRAMFR/IS/IS2012/presentations/krips-fluxcalibration.pdf>

that they have flux densities accurately known from models, Uranus and Neptune are significantly stronger than the other calibrators, and are the best sources to characterize the instrument and calibrate its flux density scale.

The total flux densities of all observations of Uranus and Neptune during runs 9 and 10 were measured directly with aperture photometry over a large radius of $150''$ to reach saturation level

These measurements are of high quality over a broad range of observing conditions ($33^\circ < \text{elevations} < 58^\circ$, and $0.16 < \tau_{1mm} < 0.50$). An illustration of our aperture photometry is given in Fig. 22.

We emphasize that prior to summation of all the pixels within the aperture, the intensity of each pixel must be estimated from its brightness given in Jy/beam in the map provided by the pipeline (beam stands for the total beam including beam and side lobes). The brightness of each pixel must be multiplied by $dx \times dx / \Omega_{\text{true}}$ where dx is the pixel size ($1''$ in our processing) and Ω_{true} is the solid angle of the total beam, traditionally called true. We have computed the solid angle of the true beam :

$$\Omega_{\text{true}}(r_{\text{max}}) = \int_0^{2\pi} \int_0^{r_{\text{max}}} B(r) 2\pi r dr$$

where $B(r)$ is the radial profile of the azimuthally averaged brigtness over narrow annuli, dr in width, and normalised so that $B(0)=1$. We have used $r_{\text{max}} = 250''$ allowed by the size of the maps observed. Only a small fraction of the incident power is left in side lobes beyond, see Greve et al (1998) and Kramer et al (2013). This integral is derived from the general expression (e.g. Adam, 2016, §8.1.1.2 of his PhD thesis) for a brightness distribution assumed azimuthally symmetric. The excess of the true beam relative to the Gaussian beam is $\Omega_{\text{true}}/2\pi(\sigma_{\text{Gauss}})^2$, with σ_{Gauss} derived from the FWHM of each observation. These excesses have been estimated for all observations of Uranus and Neptune in runs 9 and 10 and their histogram are shown in Fig. 23 (first row of plots). The mean ratios of solid angles between the true and gaussian beams are 1.87 ± 0.16 and 1.35 ± 0.08 at 1mm and 2mm, respectively. We note these ratios are consistent with the beam efficiencies (ratio of powers between main beam and total beam) of $\sim 55\%$ at $\lambda = 1\text{mm}$ ($1/1.87 \times 100$) and $\sim 70\%$ at $\lambda = 2\text{mm}$ ($1/1.35 \times 100$) found within the same extent of $250''$. The solid angle of the true beam we have determined at each wavelength will be required to convert from Jy/beam to Jy/pixel or Jy/str. We provide their distribution and mean values in Figure 24. The solid angle of the total beam is found to be $\propto \lambda^\gamma$ with $\gamma \sim 1$ determined with these mean values at 1mm and 2mm.

Finally, we stress again that the gain curve of EMIR, although implemented in the pipeline, was not used for the processing. We have determined FWHM and Ω_{true} for each observation, and this models, at least in part, any 

change in beam shape with elevation which is usually accounted for with the gain curve of the telescope. We have further investigated the excesses $\Omega_{\text{true}}/2\pi(\sigma_{\text{Gauss}})^2$ found in plotting them versus elevation and attenuation ($\exp(-\tau/\sin(\text{elev}))$) in Fig. 23. Over the range covered by the observations between 33° and 58° , there is no correlation of these ratios with elevation but with attenuation ; these ratios are about 15% larger at 1mm and 11% at 2mm for small attenuation ($\exp(-\tau/\sin(\text{elev})) > 0.8$). This effect is under investigation.

7.4 Stability of the flux density scale with the primary calibrators Uranus and Neptune

The inter-run stability of the flux density scale can be characterised with the photometry of Uranus and Neptune of run 9 (february 2017) and run 10 (april 2017). We show the ratios between the measured flux densities and their reference values at 150 and 260 GHz in Fig. 25. The resulting mean ratios μ are close to unity for the three arrays as expected since the planets were used to set the Jansky scale in average over all the observations early in the processing. It is noticeable that scatters around unity in Fig. ?? are about twice smaller in the first session conducted in significantly better weather than during the second session ; precisely, stabilities for the first session are 3.6%, 2.5% and 2.9% for arrays 1, 2, 3, respectively, with opacity $\tau_{1\text{mm}}$ between 0.05 and 0.3, and, correspondingly, for the second session, are 5.3%, 6.7% and 8.6% with $\tau_{1\text{mm}}$ between 0.25 and 0.6. It is thought, at the moment, that limitations in stability are caused by residual atmospheric fluctuations in the astronomical signal and uncertainty in opacity corrections.

Nonetheless, the flux density scale of NIKA2 is found to be highly stable and comparable to the level achieved by other modern instruments, e.g. SCUBA2 (Dempsey, 2013). The other limitation of the scale is absolute calibration that depends on the accuracy of the Moreno's model which is estimated to be 5% in the millimeter wavelength range. Hence, in combining both limitations, the total uncertainty of calibration with NIKA2 is 10% in mediocre atmospheric condition and better than 6% in fair condition.

We have plotted the flux density ratios versus elevation, opacity and attenuation in Fig.26 for Uranus and Neptune. No correlation is apparent. We stress that no gain curve was applied in processing the data but the solid angle of the total beam (true beam) was determined for each observation. This models any changes in the beam caused by telescope surface deformation and atmospheric conditions.

Finally, correlations between flux density ratios of the three arrays are shown in Fig. 27, separately for runs 9 and 10. Highest correlations are found between arrays 1 and 3.

Table 8: Reference flux densities of calibrators.

	flux densities (Jy)	
	A1 & A3 260GHz	A2 150GHz
MWC349	2.03	1.49
NGC7027	3.61	4.42
CRL2688	3.03	0.83

7.5 Stability of the flux density scale with three secondary calibrators

We have extended this analysis to all the secondary calibrators NGC7027, MWC349, CRL2688 observed during run 9. As for the planets, the observations were processed with the pipeline including line-of-sight opacity. Aperture photometry was carried out and the solid angle Ω_{true} estimated from each map. Four observations of secondary calibrators were discarded because aperture photometry failed to converge. The remaining 34 observations provided flux densities on the three arrays that were compared to their reference flux densities given in Table 8. Their ratios were plotted in Fig. 28 in time order. All measured flux densities of CRL2688 were too low at 1mm and 2mm, and its reference flux densities in Table 8 had to be decreased by 10% at 1mm and 25% at 2mm to yield the ratios shown in the Figure. All measured flux densities of NGC7027 at 1mm were also too low and its reference flux density had to be decreased by 15% at 1mm. All measured flux densities of MWC349 were too high at 1mm and its reference flux density had to be increased by 5% at 1mm.

Overall, scatters in the flux density scales of the three arrays with secondary calibrators are larger than with the stronger planets Uranus and Neptune. They are 14% for array A1, 7% for array A2, and 18% for array A3, during run 9. It is thought that in our treatment with aperture photometry the solid angle Ω_{true} estimated from each map is more uncertain because secondary calibrators are fainter than the planets.

We have plotted the flux density ratios versus elevation, opacity and attenuation in Fig.29 for three secondary calibrator. A slight correlation with attenuation may be apparent ; flux densities tend to be 10-15% higher for low attenuation > 0.8 , unlike for Uranus and Neptune. It is under investigation.

Color-correction have not been done yet for the secondary calibrators with their spectral indices α different from $\alpha = 1.6$ for the primary calibrators Uranus and Neptune.

7.6 Calibration stability across the run

8 Noise description: TOI and maps

8.1 Dark detectors at 1 mm

8.2 Dark tests

9 Detector-Detector correlation matrix

For this work we have used several decorrelation methods trying to identify possible multiple components in the noise. Notice that in the following the atmospheric signal will be considered simply as correlated sky noise. The main decorrelation methods used are:

CM Common mode decorrelation. We search for a common mode template using all detectors of the same array. To avoid bias from bad detectors we consider the median common mode.

PCA Principal Component Analysis. For each NIKA2 array independently we decompose the covariance matrix in principal components. From those we derive up to 10 independent templates corresponding to the largest eigenvalue values.

BC Best correlated pixels. For each detector in a given array we identify those detectors which are more correlated to it (a minimum of 14). Using those detectors we compute a common mode as in method CM.

ALL All detectors. For each detector of a given array we use all other detectors of the same array as templates and perform a linear fit.

We present in Figure 33 the detector noise correlation matrices computed for the N2R7 dark scan 20161211s299 for the three arrays (A1, A2, and A3 from left to right). From top to bottom we present the correlation matrices for the raw data (no decorrelation), and for the CM, PCA, and BC decorrelated data. For each array the extent and name (from letter A to T) of the electronic boxes is indicated on the left of the figure. Notice that each electronic box consists of 5 subbands.

In the case of the raw data we observe very different structures for the three arrays. In arrays A1 and A2, we observe significant structure going from very correlated detectors to fully uncorrelated ones. This is observed even within a given electronic box or even between detectors from the same electronic subband. By contrast in A3 the detectors seem to be fully correlated. After CM decorrelation we observe that there is still significant

correlation and anti-correlation for some detectors. In particular we observe a very clear pattern in A2 for electronic box A. In the case of the PCA decorrelated data the correlation matrix becomes much more diagonal although still shows significant level correlation within electronic subbands. We also notice that using the BC decorrelation improves with respect to the CM decorrelation but it is worse than the PCA case. These results tends indicate various electronic or detector related noise components.

In Figure 34 we show the noise correlation matrices for the N2R7 faint source scan 20161213s72. As expected the raw data noise correlation is dominated by atmospheric noise and we observe full correlation between detectors. After decorrelation the results are very similar to those found for N2R7 dark scan 20161211s299. There is residual significant correlation and anti-correlation after CM decorrelation. PCA decorrelation leads to a more diagonal correlation matrices. For the BC decorrelation the results are worse (more residual correlation and anti-correlation) and close to those of the CM decorrelation. As before there are good indications of multiple electronic-detector noise components. It is interesting to note that the detector-electronic noise correlation patterns seems to be the same for dark tests and for sky data.

We have repeated the same analysis on scans of the N2R4 both for dark tests, scan 20160504s97, and faint sources, scan 20160313s87. We find few significant differences with respect to previous results. In the case of the dark test and for the raw data, the A1 and A2 detectors seems to be more correlated. Furthermore A2 show more significant correlation after CM decorrelation for electronic boxes B and D. Array A1 show also significant residual correlation and anti-correlation after CM et BC decorrelations. For the faint source N2R4 scan 20160313s87 we observe similar behavior but the pattern of the correlation matrices are not the same that for the dark test scan.

9.1 RMS of the noise

We present in Figure 37 the rms, in Hz, of the raw (dark blue) and decorrelated (CM, blue; PCA, red; and BC, cyan), data for the N2R7 dark test scan 21612101s299. We also show for comparison the rms of the data by extrapolating the median high frequency noise (PS, violet). For the three arrays we observe that decorrelation reduces significantly the rms noise. The most efficient method is PCA as one would expect from previous results in the noise correlation matrix.

For each array the detectors are ordered by electronic box (separated by

vertical black lines in the figure) and within each electronic box by increasing resonant frequency. We observe that median high frequency noise increases with increasing resonant frequency. A similar effect is observed for the PCA and BC rms noise but for some pathological detectors or electronic boxes. While in A2 the rms noise increases monotonically with resonant frequency in arrays A1 and A3 we observe also observe fine structure within each electronic box. For array A2, electronic box A, shows significantly larger raw rms. For array A1 box K seems to have a larger number of anomalous detectors than the other boxes. In array A3 all boxes seem to be equivalent to first order. Both in A1 and A3 we find complex structure within each box, which are not present in A2.

Similar results are found for scan 20161213s72 as shown in Figure 38. However, we stress that the atmospheric emission shows significant contribution at high frequency (see PS) that is significantly reduced after decorrelation.

We have also computed the noise rms for the scans of N2R4 20160504s97 and 20160313s87. For arrays A1 and A3 the results are very similar to those for the N2R7 scans. However, we clearly observe that A2 is significantly worse in terms of misbehaving pixels.

9.2 Discussion

Using dark test measurements we have identified several noise components that require using complex decorrelation methods. Event in the case of multiple template decorrelation we find residual correlation between detectors that seems to be related to electronic subbands. Similar results are found when analyzing faint source scans. We find significant differences between N2R4 and N2R7 scans.

After decorralation using multiple template procedures we reduce significantly the rms of the noise. In the case of dark test it becomes of the level of the high frequency noise. For faint source scans we also diminish the high frequency noise, which is probably dominated by atmospheric emission. We find significant differences between the noise levels in A1 and A3, which might be explained by gain differences (to be verified). For some electronic boxes in A2 the rms noise is significantly larger than for the others. For the three arrays we find increasing noise with increasing resonant frequency withing each electronic box. This is probably related to the difference of gains between subbands in the electronics. Furthermore, we find in A1 and A3 extra low frequency structures in the rms which are not identified yet.

10 Sensitivities

The specs/goals “NEFD on X % of pixels” should be understood as : we have XX% valid pixels, and with these pixels, we have an NEFD of YY. We should not discard some fraction of our pixels and estimate an NEFD on this subset.

HLS091828 is moderately faint source, expected to be below 100 mJy at 1mm and XX mJy at 2mm check values in NIKA1 paper + use SED for predictions in NIKA2's bands. This source was chosen for its flux and its availability during Run9 for long integration. It has been observed for XX hours in total over three nights.

10.1 Data processing

The data were decorrelated using the XXX method... The scans have been combined with standard inverse noise weighting. The noise in each map pixel is derived from the rms of the background corrected for the number of observations per pixel.

10.2 NEFD Methods 1 and 2: deep integration

These data can be used to derive the NEFD in several ways. One is to fit the evolution of the uncertainty on the flux of the source σ_ϕ with the integration time. Another one is to produce jackknife maps with the data and to measure the uncertainty on the flux in the end, while estimating the time of integration. Results are summarized in Tab. 10.2.

Fig. 41 shows the decrease of the uncertainty on the measured flux at the center of the map as a function of time. We either fit a power law or fix the power law to -0.5 and fit only the amplitude. Uncertainties on these values have been estimated via a bootstrap method: we randomize the scans and derive the standard deviation of the average of n scans for any n between 1 and the total number of scans. This gives us an estimate of the uncertainty on σ_ϕ for a time of integration corresponding to n scans. Strictly speaking, all the scans do not have the exact same duration, but the difference is negligible here.

33.325263 5.2024647 28.397230 4.5723151 21.143376 4.1538804 5.7628233
3.3094792

10.3 NEFD Method 3: scan NEFD vs opacity and air mass

In this section we investigate the astronomer NEFD as a function of the atmospheric opacity and air mass. Figure 42 shows the measured NEFD,

Array	Free power law	Fixed power law $t^{-0.5}$	Jackknife	Instrument
A1	$47.9 \text{ mJy.s}^{-0.54}$	$37.9 \text{ mJy.s}^{1/2}$	$35.6 \text{ mJy.s}^{1/2}$	$33.3 (5) \text{ mJy.s}^{1/2}$
A2	$5.2 \text{ mJy.s}^{-0.51}$	$4.8 \text{ mJy.s}^{1/2}$	$5.7 \text{ mJy.s}^{1/2}$	$5.8 (5) \text{ mJy.s}^{1/2}$
A3	$38.9 \text{ mJy.s}^{-0.54}$	$30.6 \text{ mJy.s}^{1/2}$	$30.4 \text{ mJy.s}^{1/2}$	$28.4 (4) \text{ mJy.s}^{1/2}$
A1 & A3	$28.5 \text{ mJy.s}^{-0.53}$	$23.6 \text{ mJy.s}^{1/2}$	$22.4 \text{ mJy.s}^{1/2}$	$21.1 (3) \text{ mJy.s}^{1/2}$

which we refer to as astronomer NEFD, for the 1 and 2 mm as a function of the measured atmospheric background in terms of $\tau / \sin(El)$. The atmospheric opacity was computed as discussed in Section 3. We observe that the increase of the astronomer NEFD is in agreement with what we would expect for background dominated sensitivity. We observe however some significant deviations from the curve. To investigate this issue we also show in Figure 43 the evolution of the background corrected NEFD, hereafter instrument NEFD, across the N2R9 campaign for arrays A1 (blue), A3 (green) and A2 (cyan), and for the combination of A1 and A3 (red). We globally observe stable NEFD across the run, with A1 sensitivity being worse than for A3. We also show the measured instrument NEFD as a function of the flux of the source in the 1 mm channel in Figure 44. We observe that the observed deviations in the instrument NEFD correspond mainly to the large flux source scans. This is more obvious in Figure 45 where we present the histogram of the measured NEFD for 2 mm of pwv and at a elevation of 60 degrees, hereafter, reference NEFD, for the 1 and 2 mm channels.

11 Summary of performance

The main measured parameters that define the actual NIKA2 performances are gathered in Table 9.

The performance parameters given in Table 9 are splitted in two different lists: first, the main characteristics, as defined in the MOU, are listed in Table 10, second, other parameters, which are derived from the instrument characteristics described in the MOU, and that need to be characterized to complete the commissioning phase are given in Table 11. Table 11 is constructed from the ‘secondary’ and ‘tertiary’ tables of Samuel’s summary document.

A Reference to technical documentation

This paragraph reviews the status of the technical documentation that should be delivered to the collaboration by the NIKA2 consortium and the IRAM, as defined in the MOU.

A.1 Consortium-lead documentation

- Plan of the cryostat: 3D model (e.g. STEP, Solid Works, etc.) and plans as built (e.g. PDF)
- List of hardware components (per module)
- Optics filtering components. [Consortium].
- Cryogenics system characteristics with basic and standard operating procedures (see section 6.3).
- Cryogenics monitoring and diagnostic tools plus procedure to contact a cryogenist from the consortium who is mandated to help IRAM in case of problem with the cryostat.
- Electronics cards characteristics, implantation plans, and operating procedures.
- Programmable electronics.
- Network needs (architecture, data rates, speed, memory, synchronization accuracy, internet access, storage, backup, archiving, etc).
- Software for instrument control and data acquisition (Camadria), aimed at general users.

A.2 IRAM-lead documentation

- Optics imaging system characteristics and calculations
- Observers interface: PaKo functions specific to NIKA2, plus useful scripts
- Automated on line data processing tools. [IRAM lead, consortium input].
- Off line data processing software. [IRAM lead, consortium input].
- Cook book (for external users: including a short description of NIKA2 setup, check list and procedure to use the instrument at the telescope). Can be provided at the end of instrument commissioning. [IRAM, consortium input].

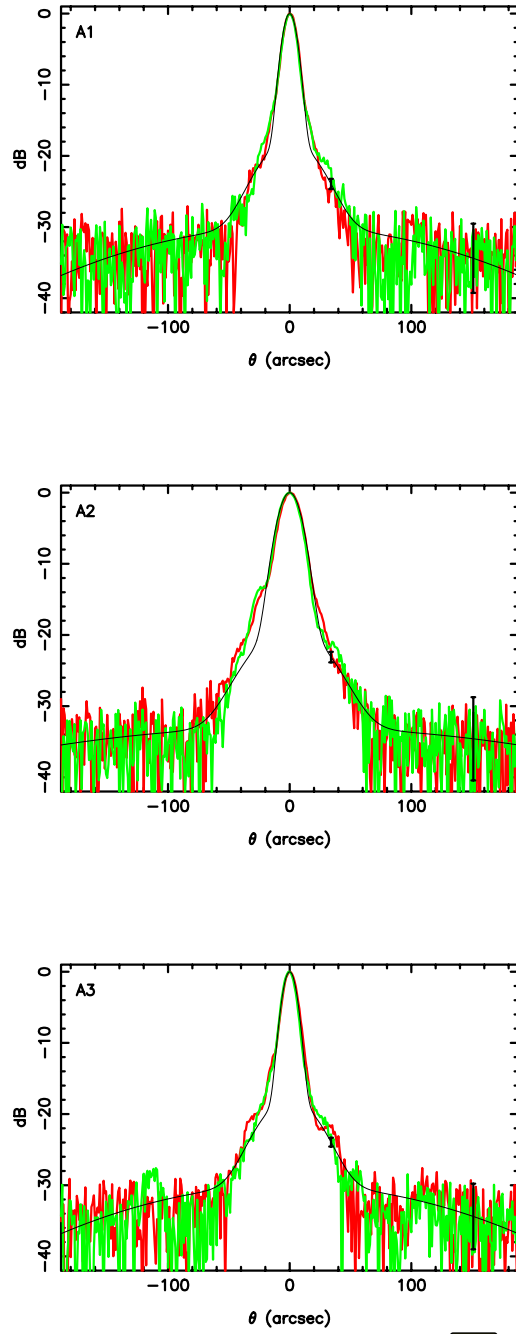


Figure 18: Two orthogonal cuts through the beam are shown in red and green and a best fit model made of three Gaussians is superimposed in black. These cuts were obtained from the high quality map of Uranus on 2017 January 25th. The main beam starts to depart from the first Gaussian at -12dB.



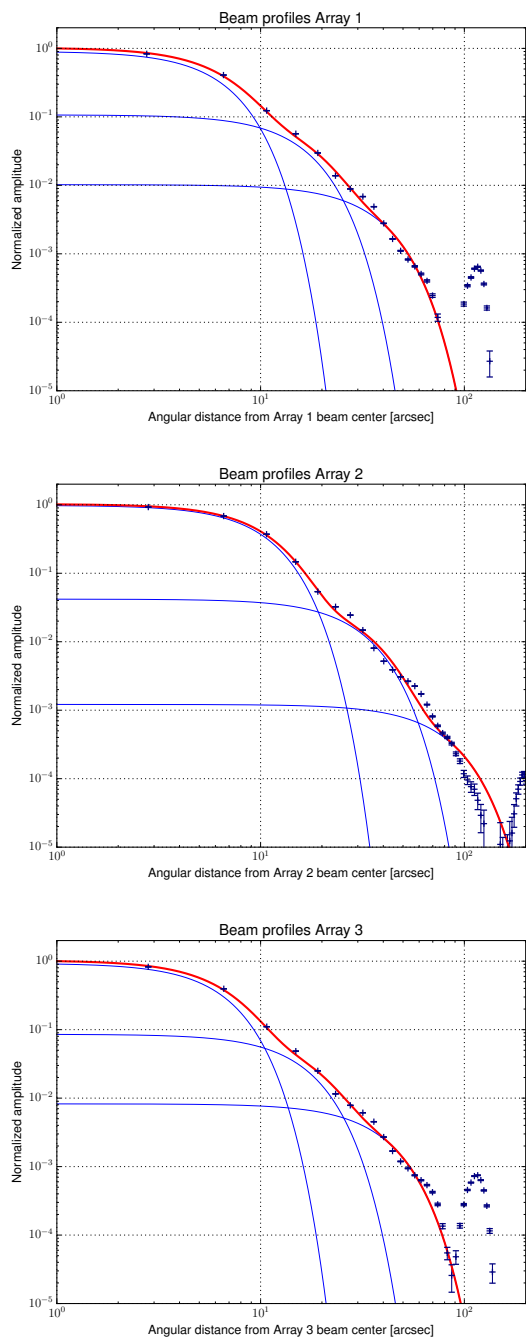


Figure 19: Beam profiles for array 1, 2, and 3.



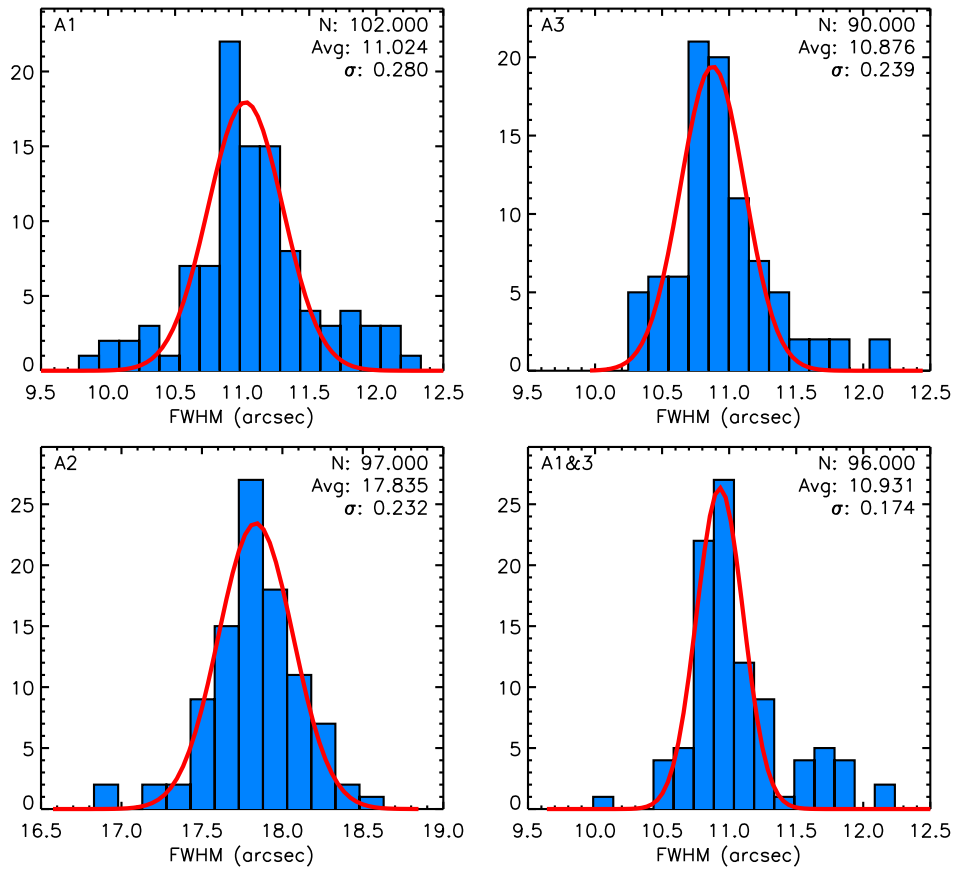


Figure 20: Distribution of the main beam FWHM estimates using 2D Gaussian fits on N2R9 and N2R10 $8' \times 5'$ OTF scans of bright point sources

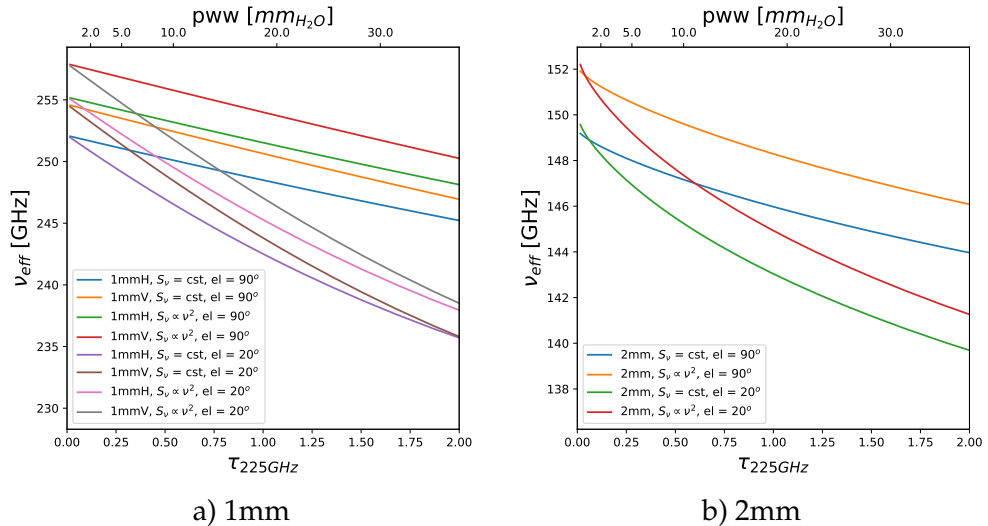


Figure 21: Effective frequency as a function of the sky opacity. The effective frequency (see text) have been computed for two source spectra (RJ and constant), and for two elevations.

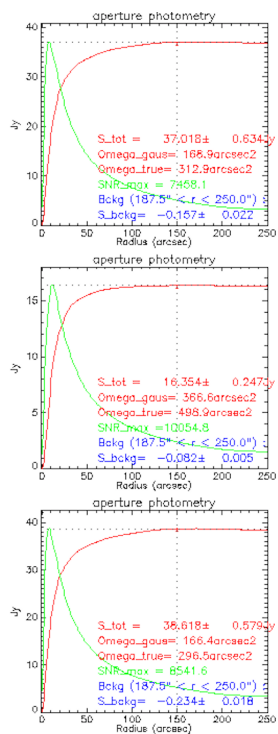


Figure 22: Aperture photometry of Uranus observation 20170227s308 on array 1, 2 and 3 from **left to right**. The photometric curve in red saturates at about the radial distance of 150''. (Green curve is the SNR in individual annulus

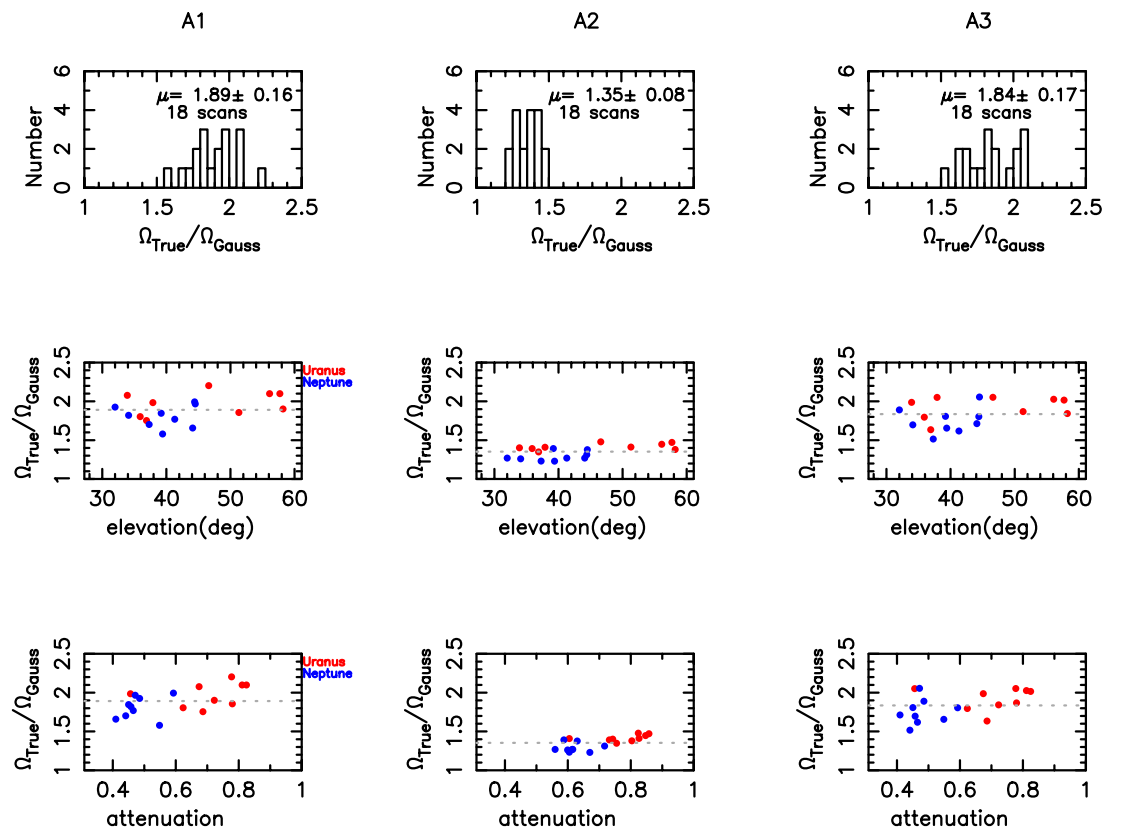


Figure 23: Solid angle excesses between the true and gaussian beams for all observations of Uranus and Neptune during runs 9 and 10.

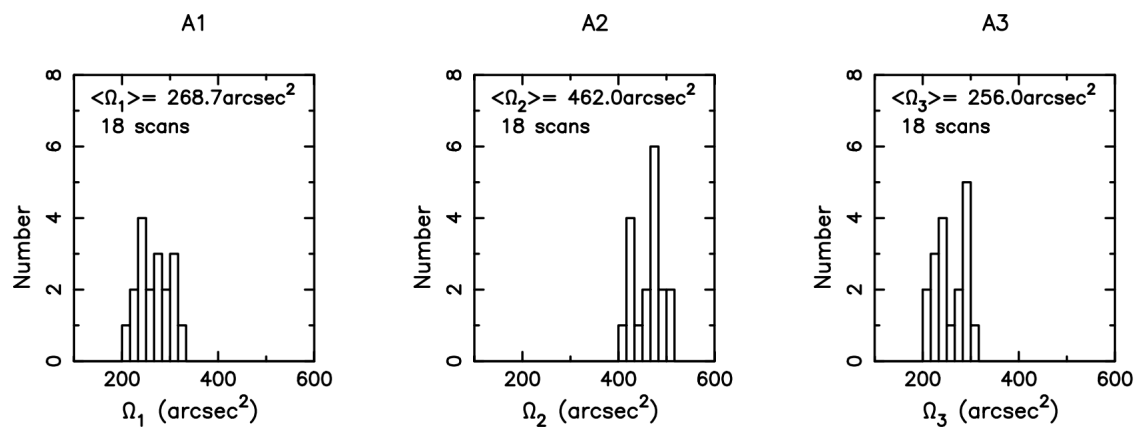


Figure 24: Solid angles of the true beams for the three arrays determined with Uranus and Neptune during runs 9 and 10. $\langle \Omega_{1,2,3} \rangle$ in plots are mean values.

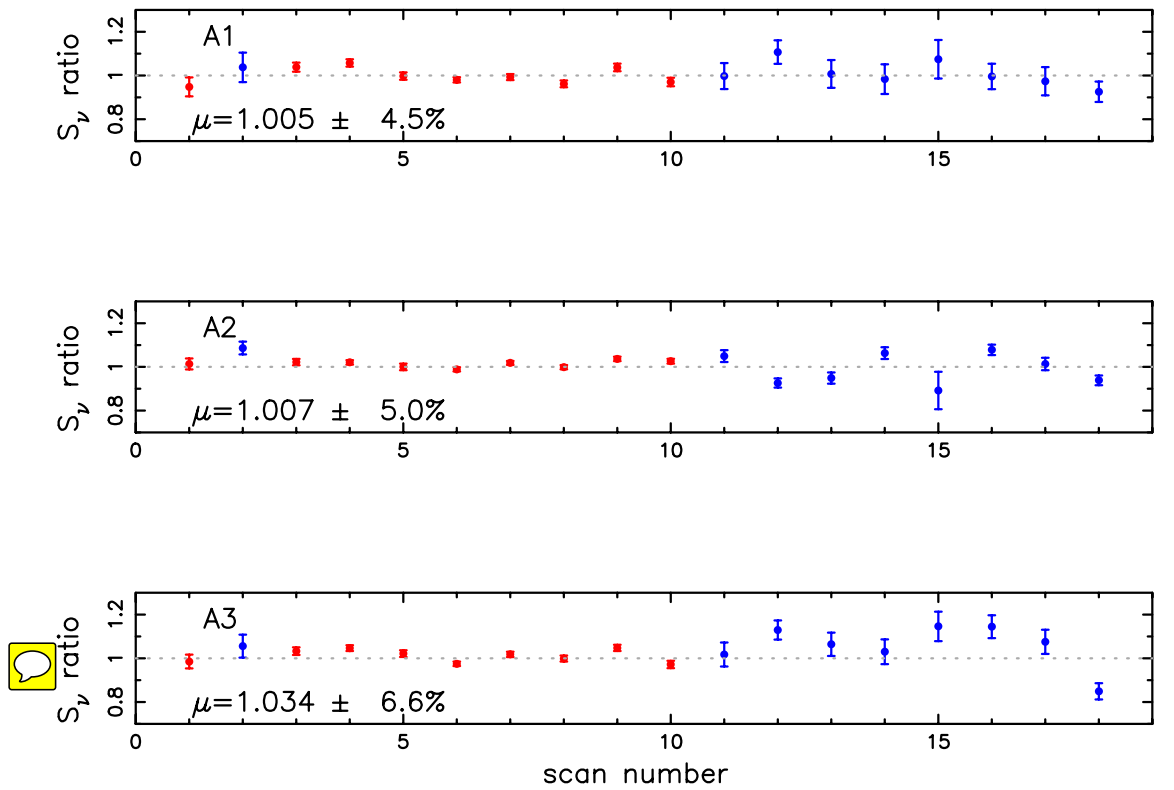


Figure 25: Stability of the flux density scale with the primary calibrators Uranus (red) and Neptune (blue) : ratios between their measured and reference flux densities during run 9 and 10. Mean ratio μ and scatter are provided for each array. Observation numbers are time ordered : 1 to 10 are 23-28 february 2017 and 11 to 18 are 19-25 april 2017. Neptune was hardly visible at the telescope during run 9, and Uranus was not visible during run 10. Observations are beammaps (22 minutes) or sequence of 4 consecutive 4 minute long ofts (16 miunutes) that are comparable in integration times.



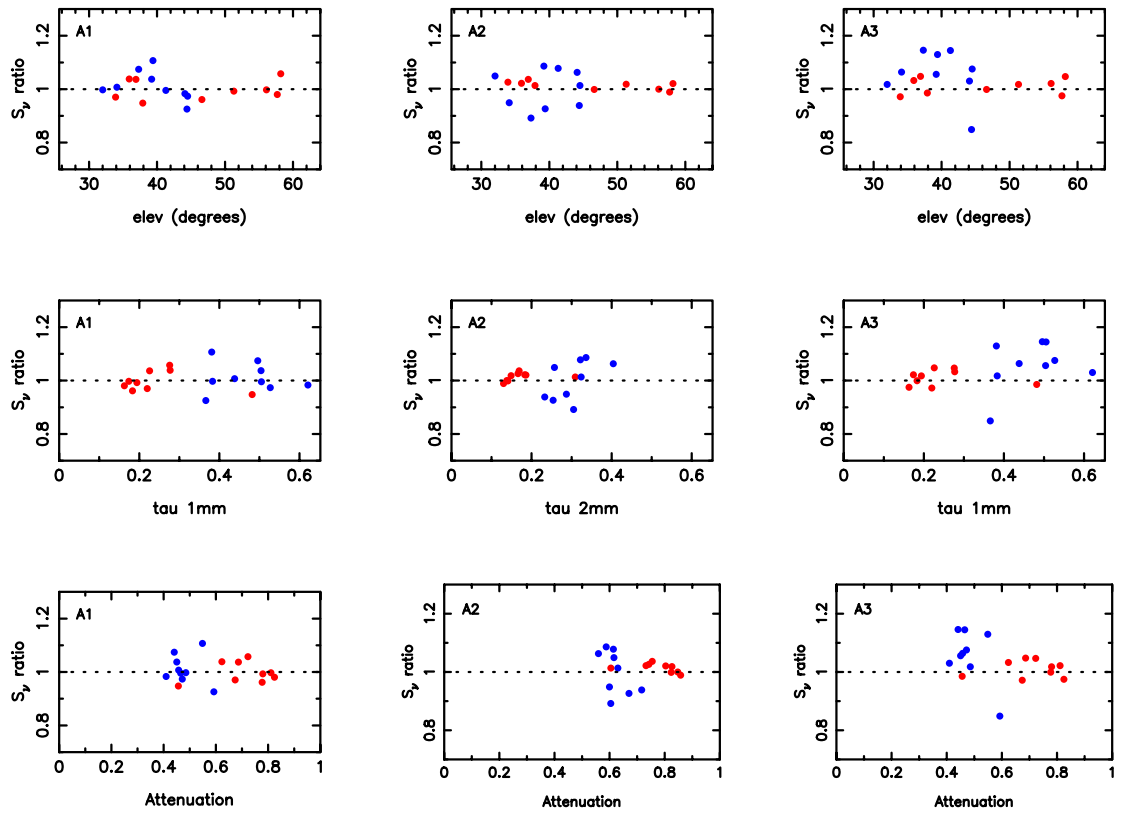


Figure 26: Flux density ratios versus elevation, opacity, and attenuation ($\exp(-\tau / \sin(\text{elev}))$) for Uranus and Neptune. No correlation is apparent with attenuation.

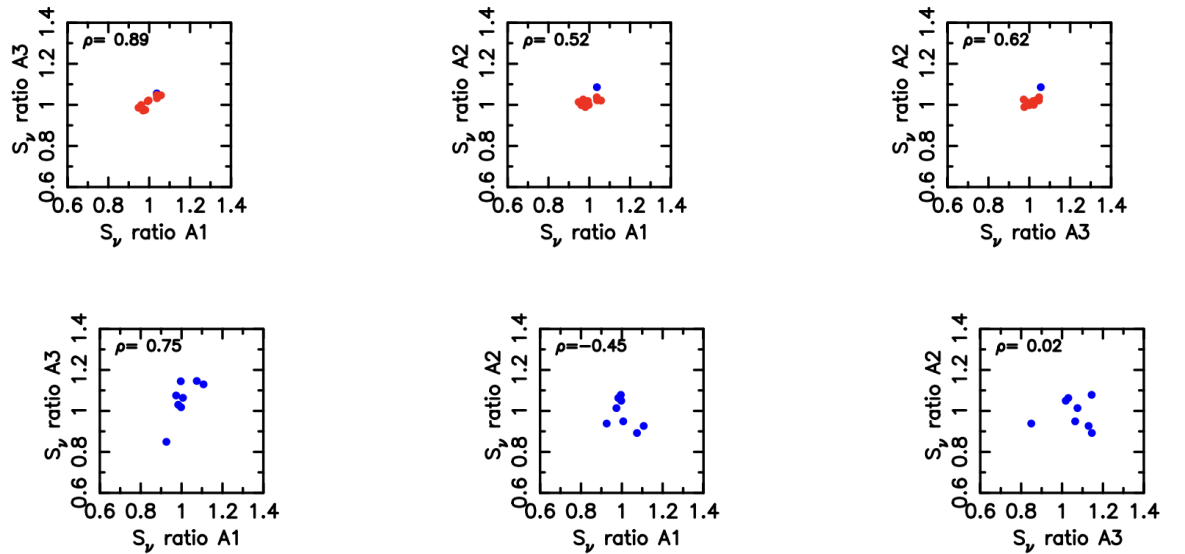


Figure 27: Correlation plots for the flux density ratios between the three arrays shown separately for run 9 (fair atmospheric condition) and run 10 (mediocre condition). Correlation coefficients ρ are given.

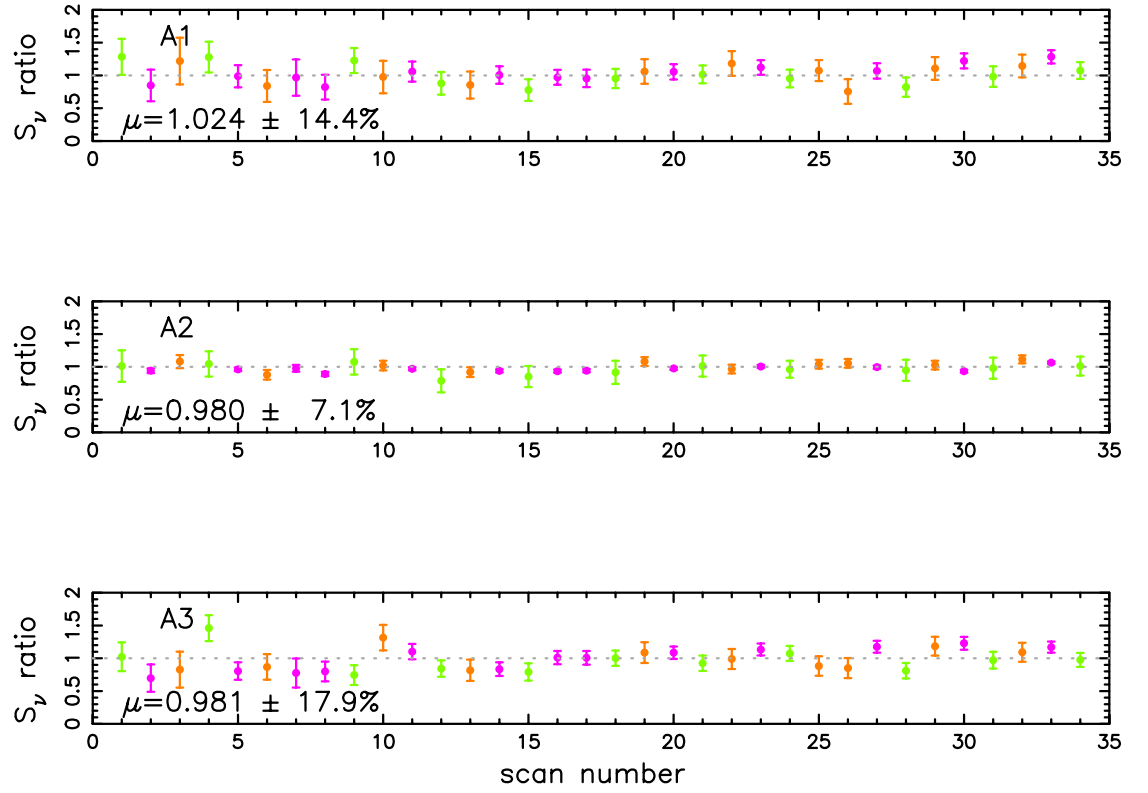


Figure 28: Stability of the flux density scale with the secondary calibrators MWC349 (brown), NGC7027 (purple) and CRL2688 (green) : ratios between their measured and reference flux densities during run 9. Mean ratio μ and scatter are provided for each array. Scan numbers are time ordered. Each observation is a sequence of 4 consecutive 4 minute long ots (total integration is 16 minutes).



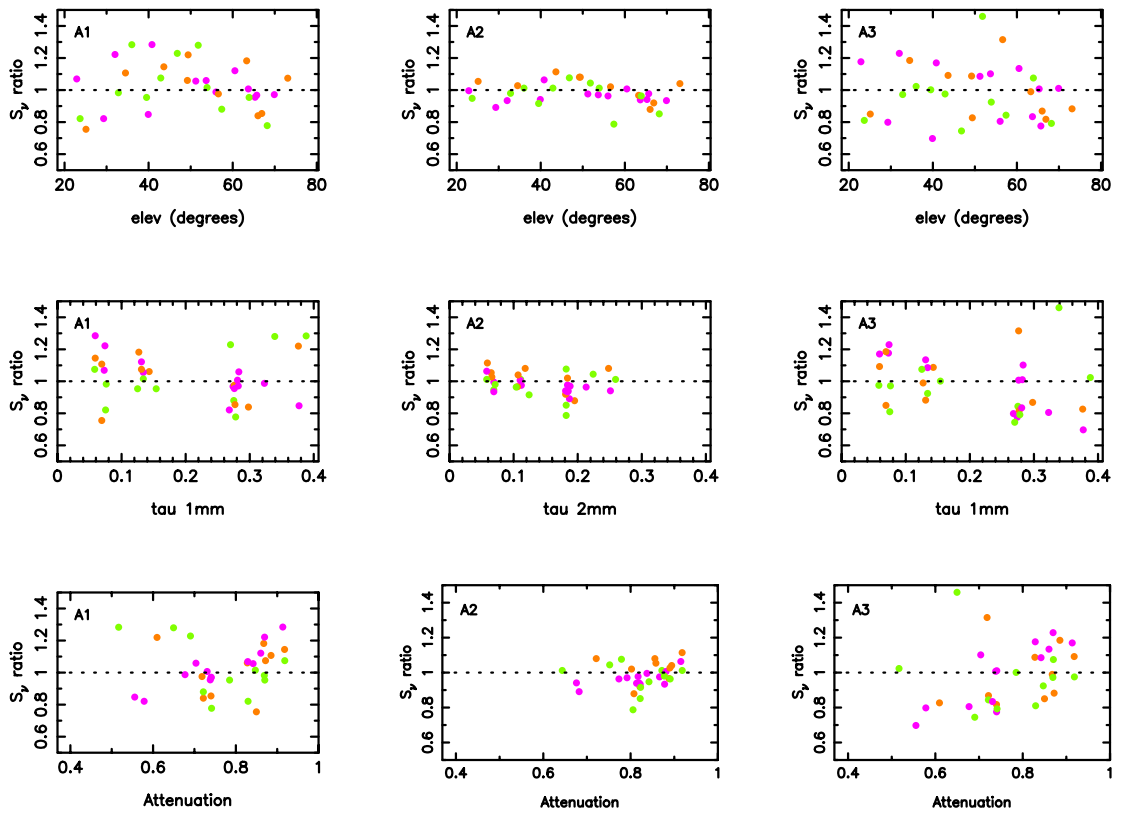


Figure 29: Flux density ratios versus elevation, opacity, and attenuation ($\exp(-\tau / \sin(elev))$) for the three secondary calibrators. A slight correlation with attenuation may be apparent ; flux densities tend to be 10-15% higher for low attenuation > 0.8 .

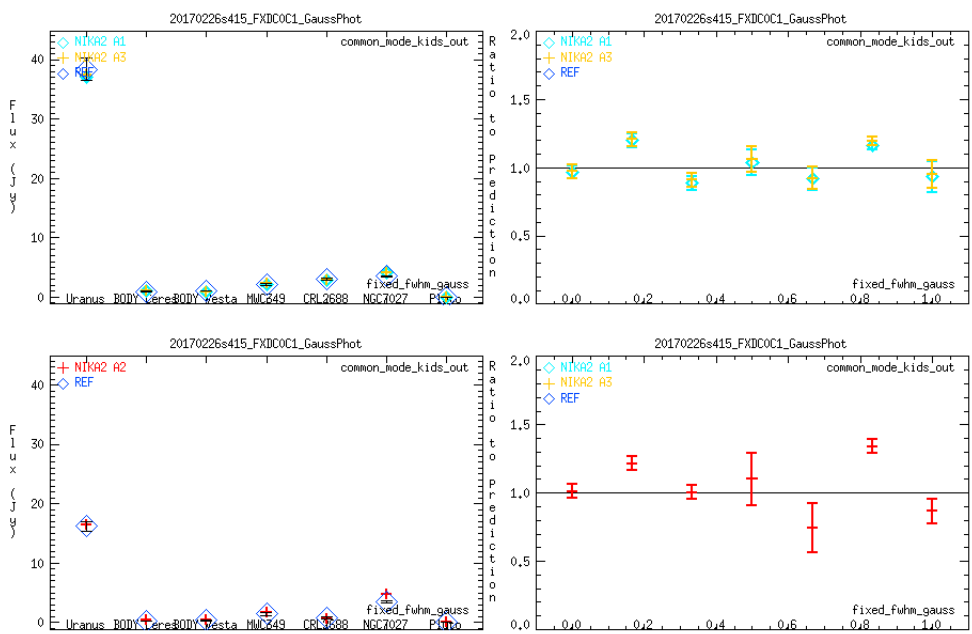


Figure 30: Decorrelation mask: 100 or 60 arcsec, KID cross-calib with fixed fwhm (12.5 and 18.5), then absolute photometry with the same fixed fwhm. Note: NGC7027 not point like and not corrected for here. Error bars from NIKA2 measurements and abs. cal. uncertainties by JFL.

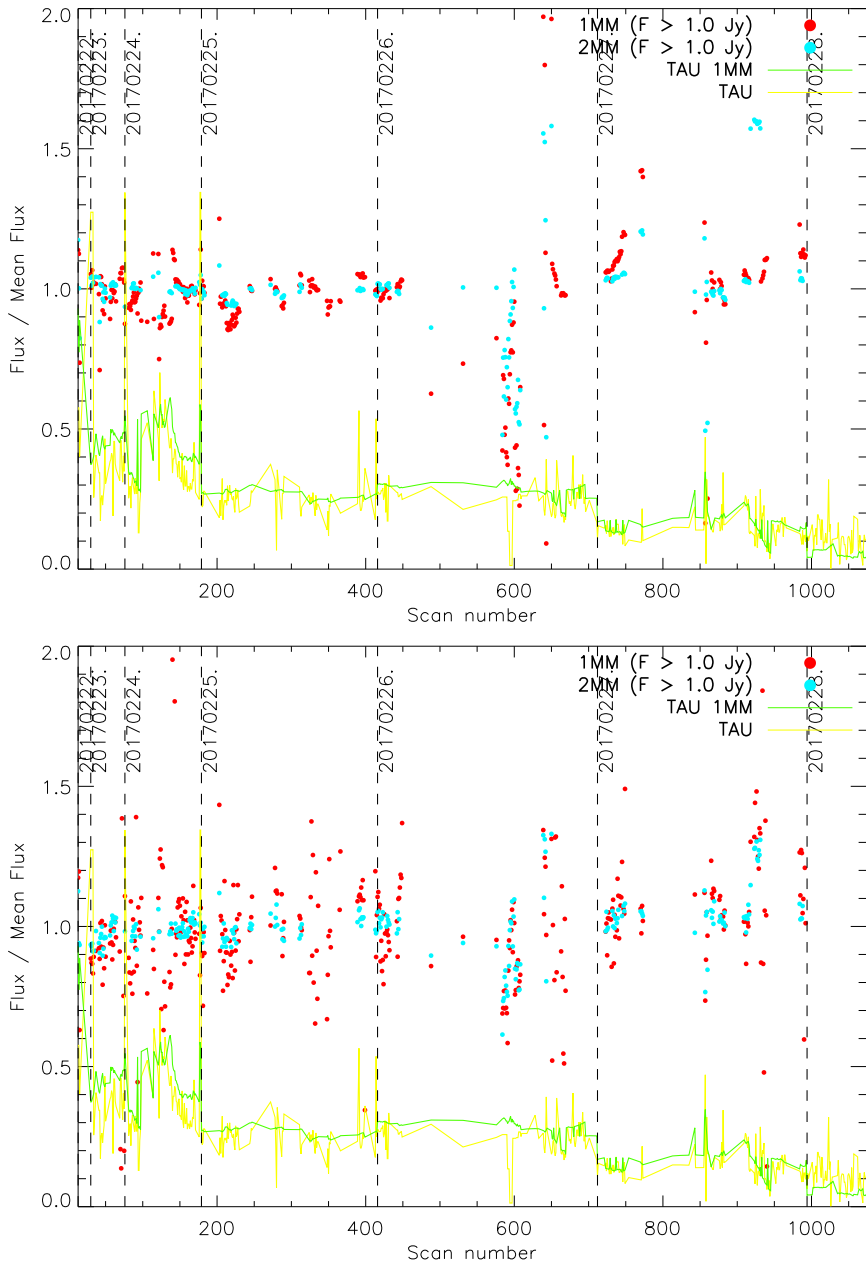


Figure 31: Ratio between the measured flux per scan and the averaged flux for all sources observed in N2R9. We considered both fixed FWHM (top) and aperture photometry fluxes for the 1 (red) and 2 (cyan) mm channels.

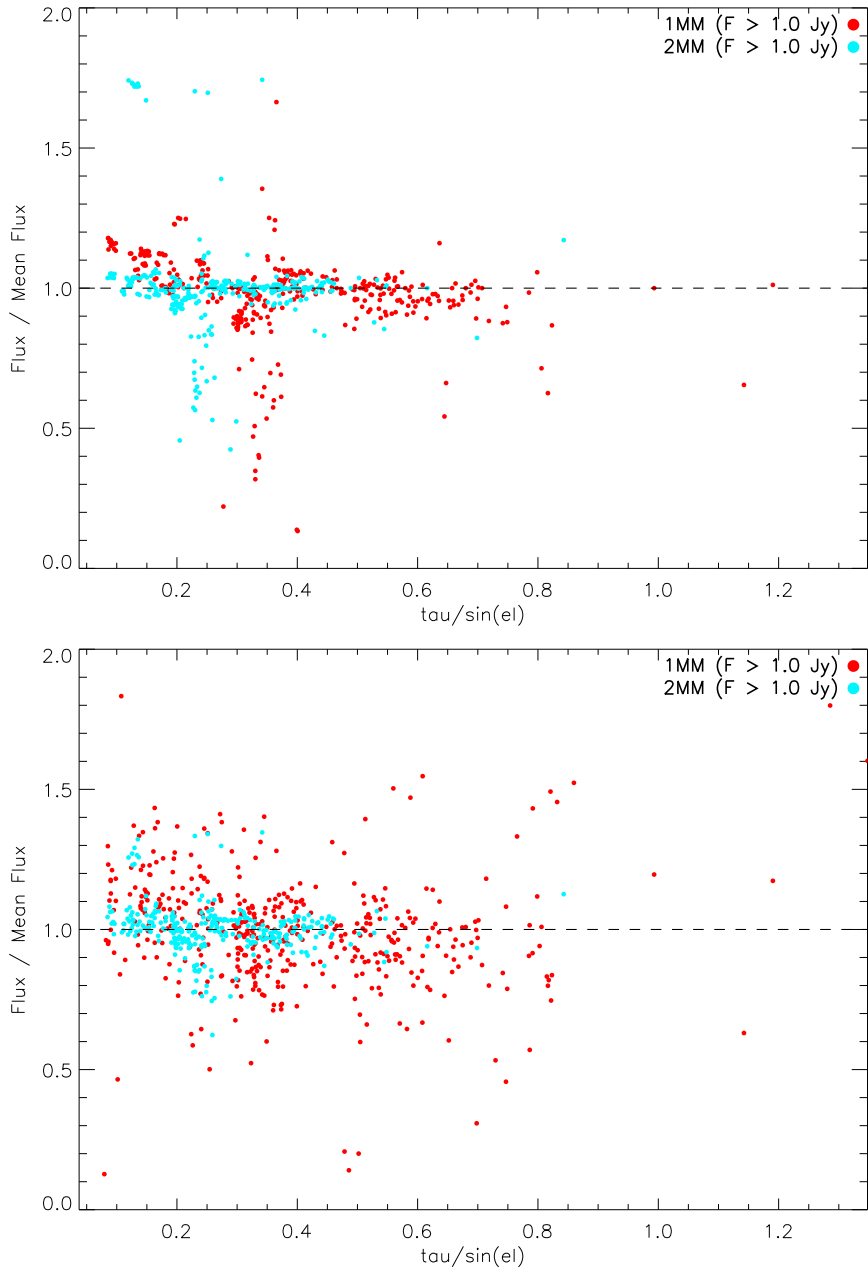


Figure 32: Ratio between the measured flux per scan and the averaged flux as a function atmospheric background for all sources observed in N2R9. We considered both fixed FWHM (top) and aperture photometry fluxes for the 1 (red) and 2 (cyan) mm channels.

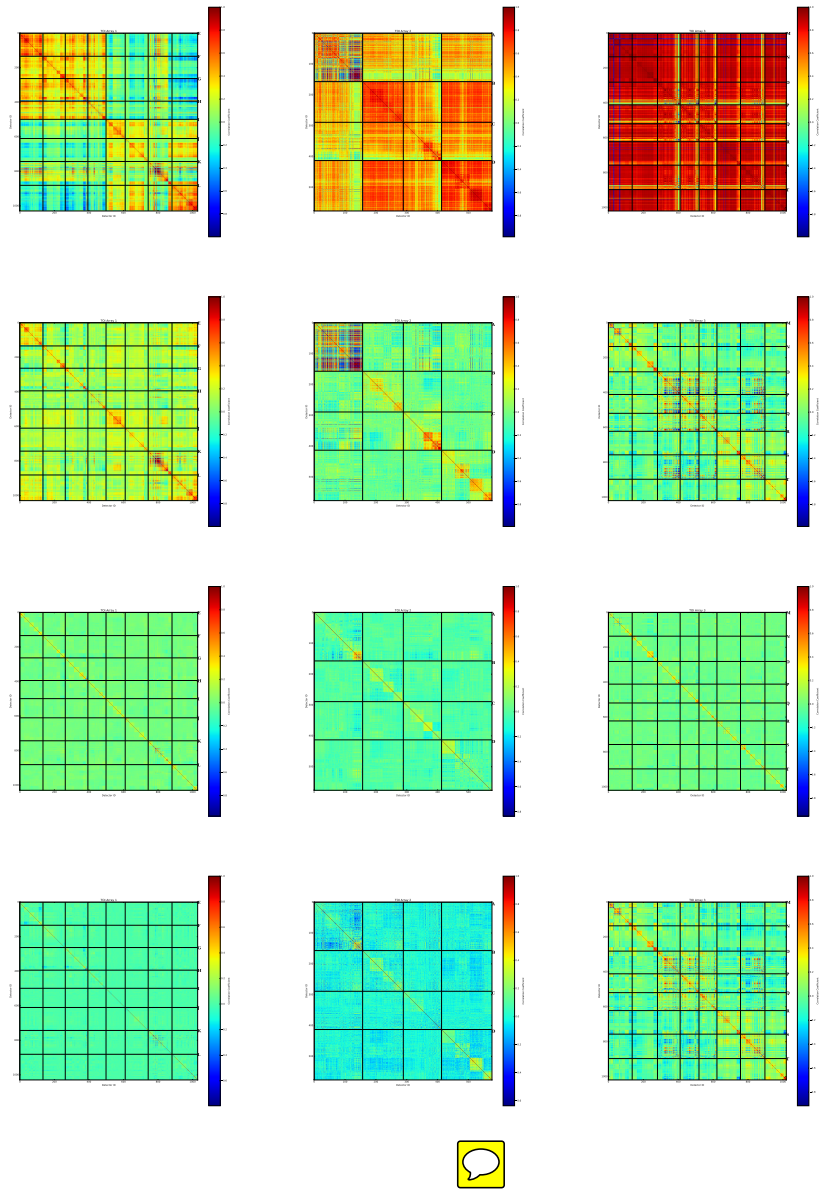


Figure 33: From left to right correlation matrices for the three NIKA2 arrays (A1, A2, and A3) for scan 20161211s299. From top to bottom we present the correlation of the raw data, after CM, PCA and BC decorrelations.

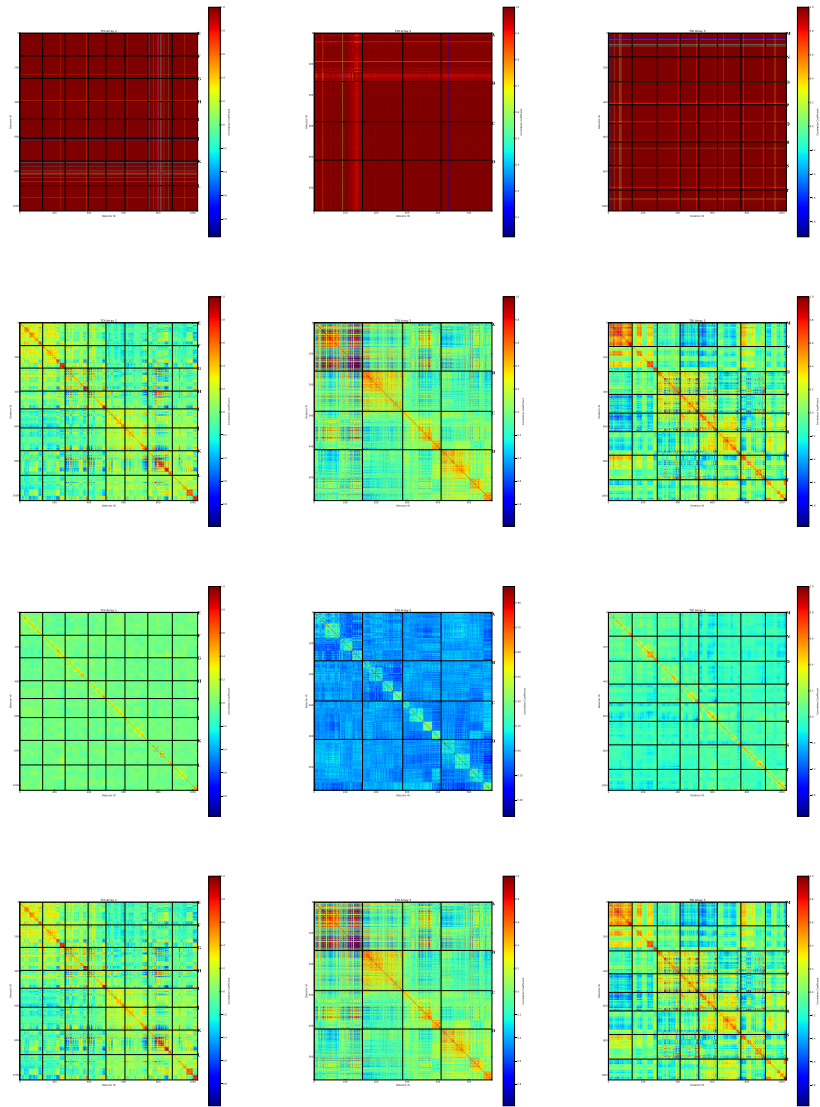


Figure 34: From left to right correlation matrices for the three NIKA2 arrays (A1, A2, and A3) for scan 20161213s72. From top to bottom we present the correlation of the raw data, after CM, PCA and BC decorrelations.

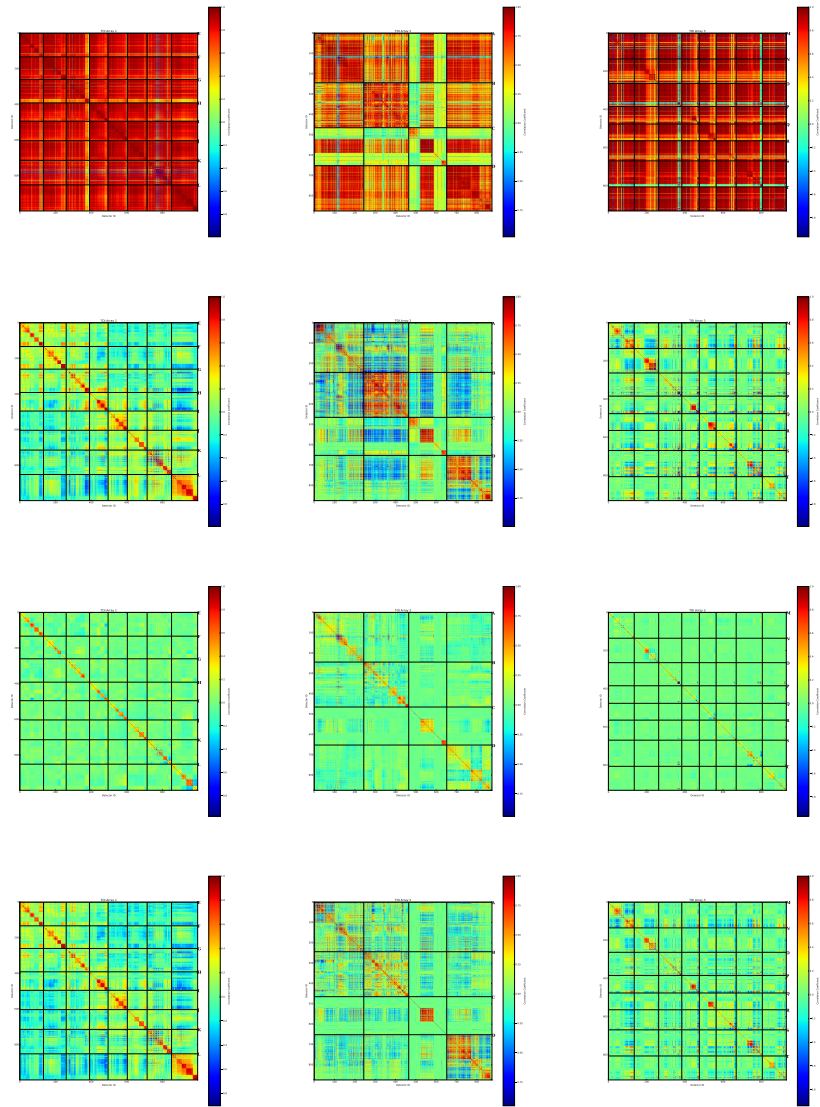


Figure 35: From left to right correlation matrices for the three NIKA2 arrays (A1, A2, and A3) for scan 20160504s97. From top to bottom we present the correlation of the raw data, after CM, PCA and BC decorrelations.

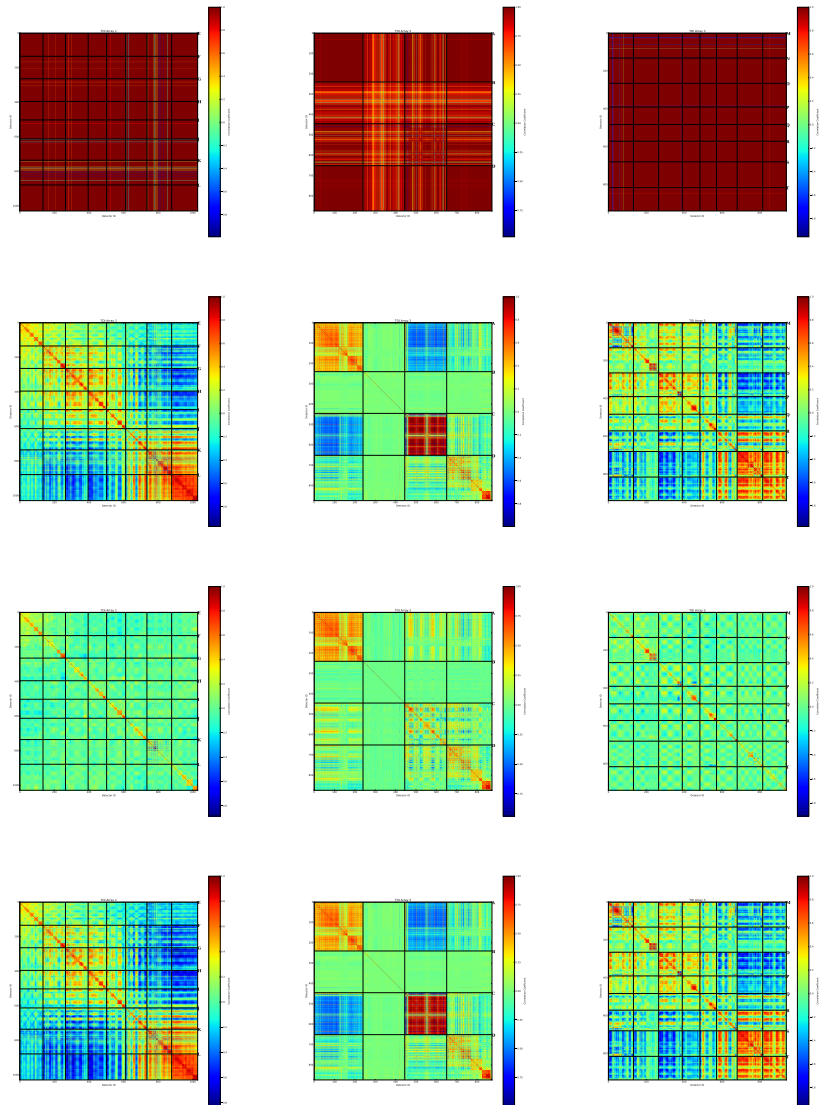


Figure 36: From left to right correlation matrices for the three NIKA2 arrays (A1, A2, and A3) for scan 20160313s87. From top to bottom we present the correlation of the raw data, after CM, PCA and BC decorrelations.

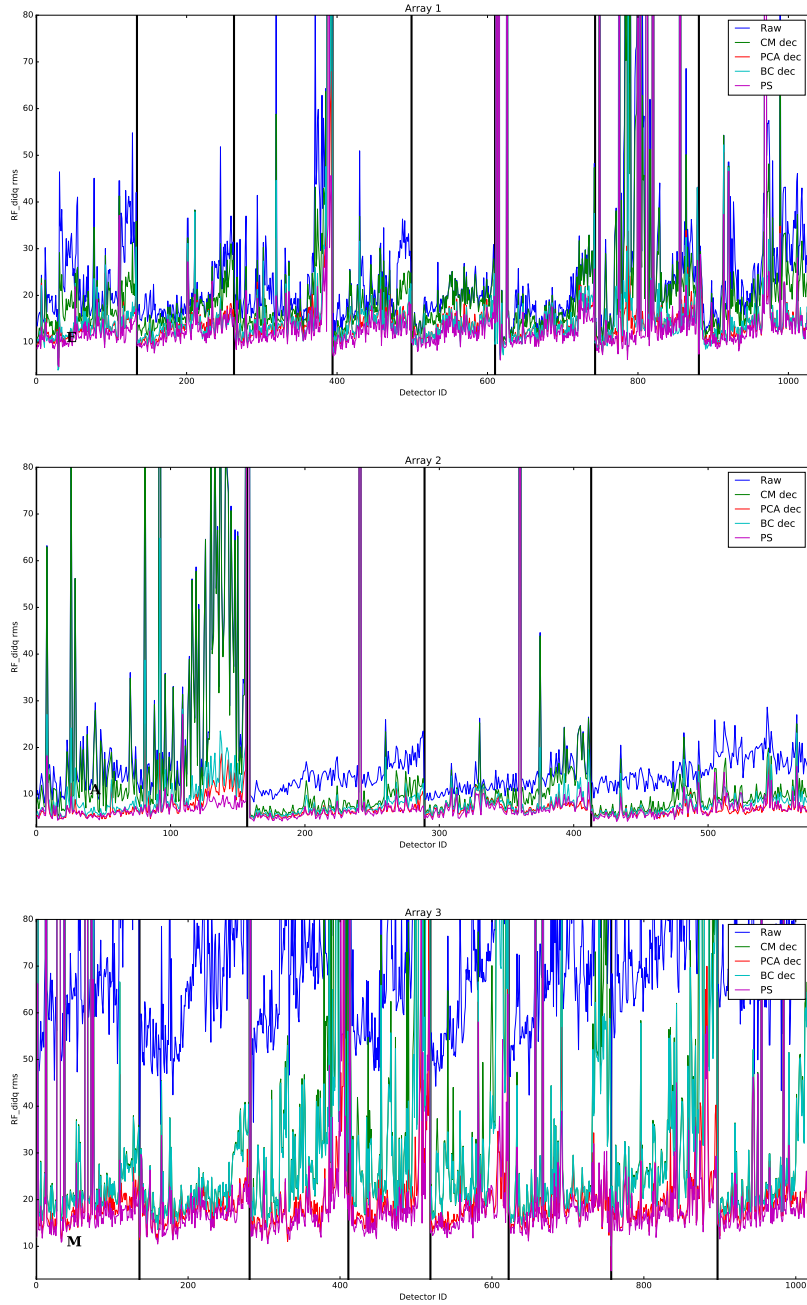


Figure 37: RMS noise for arrays 1,2, and 3 (top to bottom) for scan 20161211s299. The rms is computed for the raw data, and for the three decorrelation methods, CM, PCA and BC. The rms value for the level of white is also computed from the raw data power spectrum (PS).

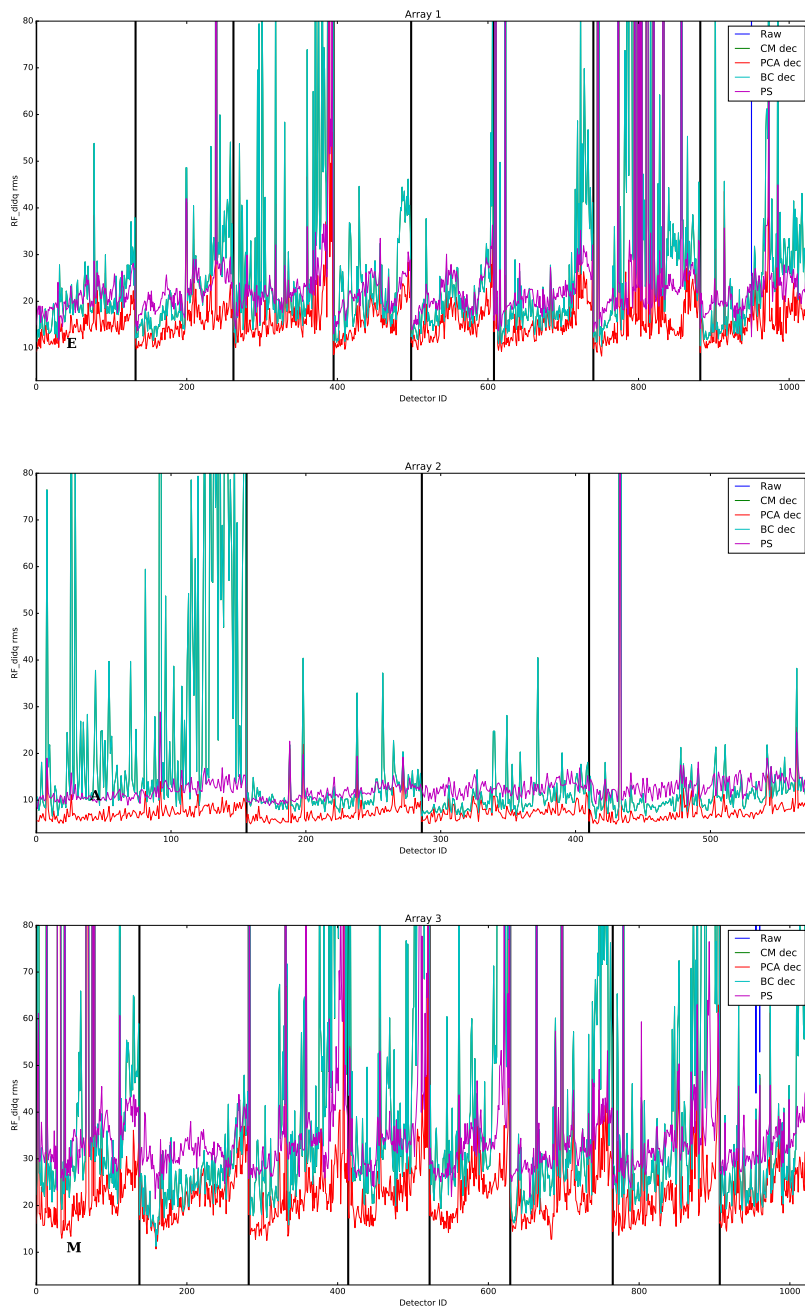


Figure 38: Same as Figure 37 but for scan 20161213s72.

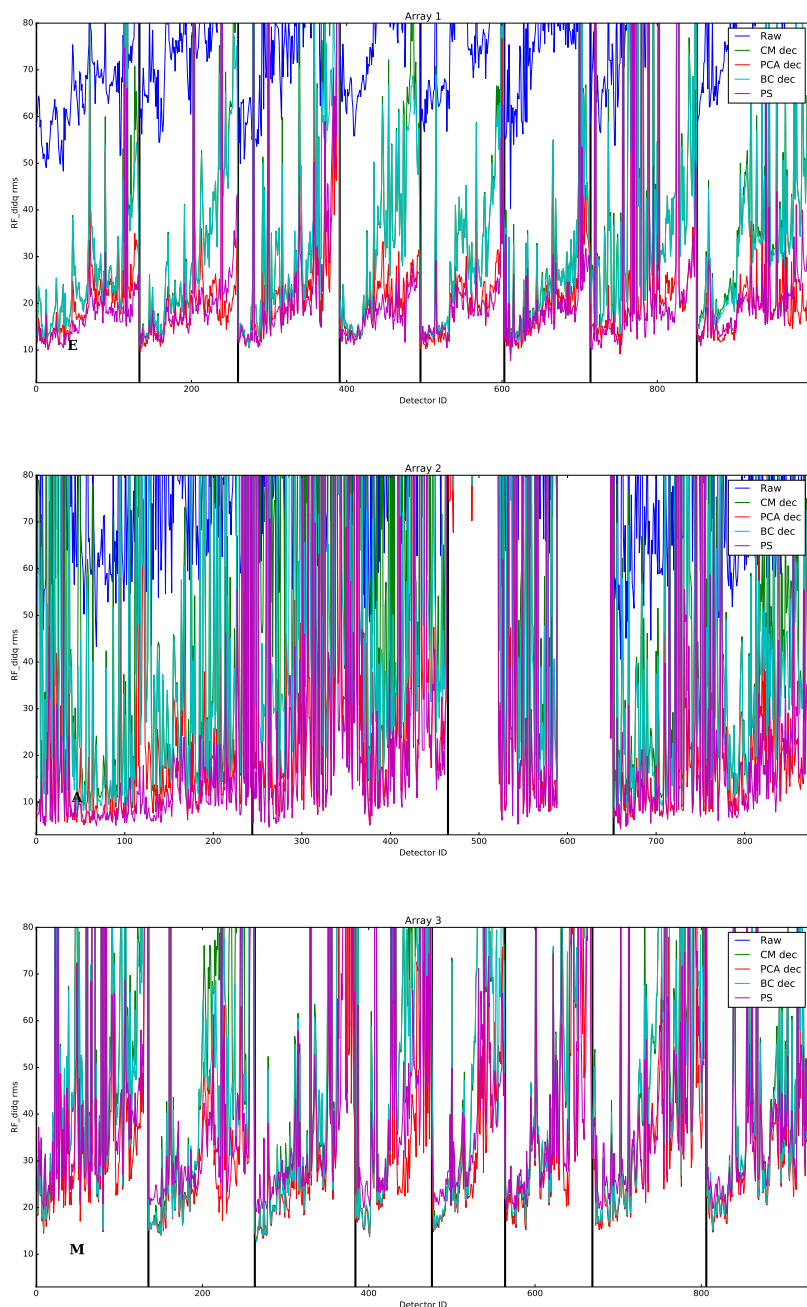


Figure 39: Same as Figure 37 but for scan 20160504s97.

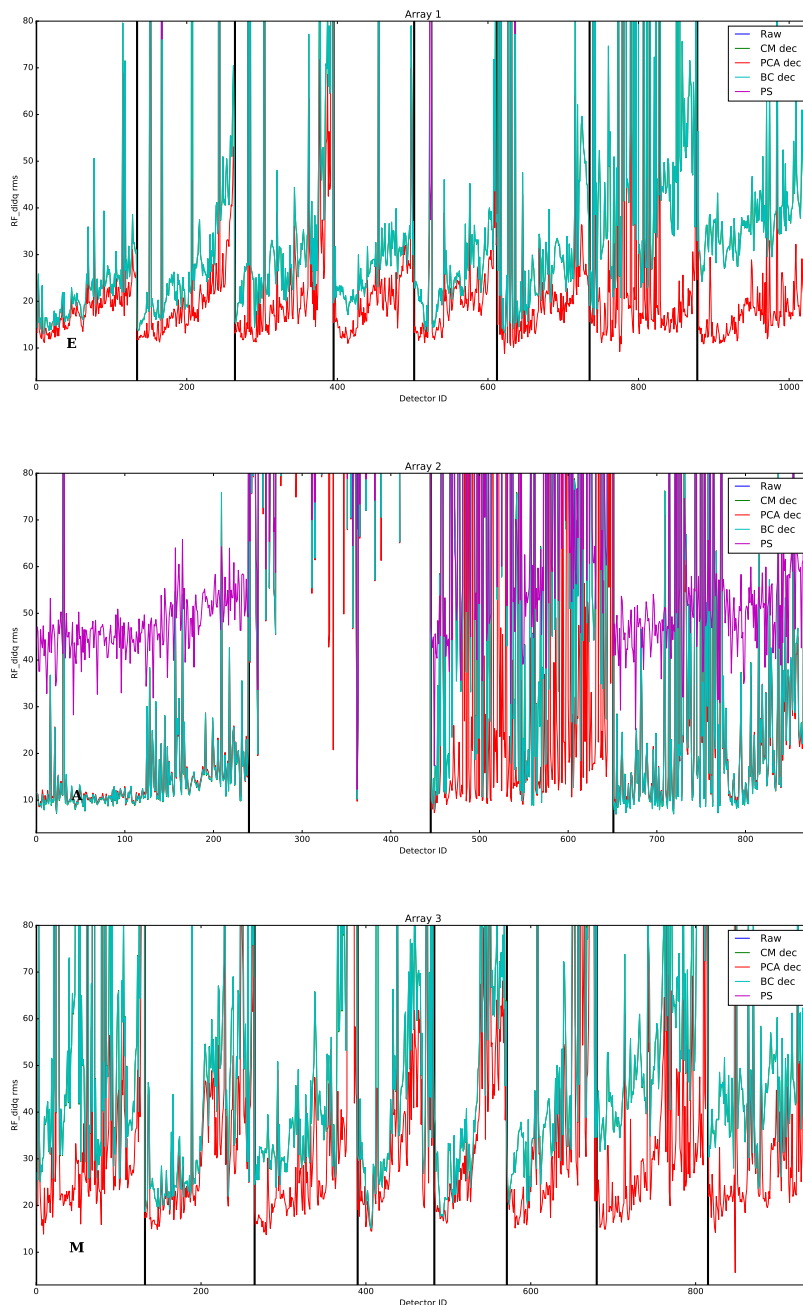


Figure 40: Same as Figure 37 but for scan 20160313s87.

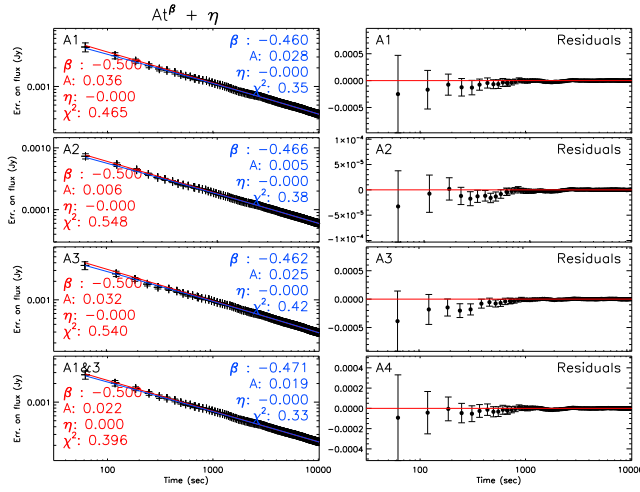


Figure 41: Kids Xcalib with fixed fwhm 12.5 and 18.5, HLS091828.

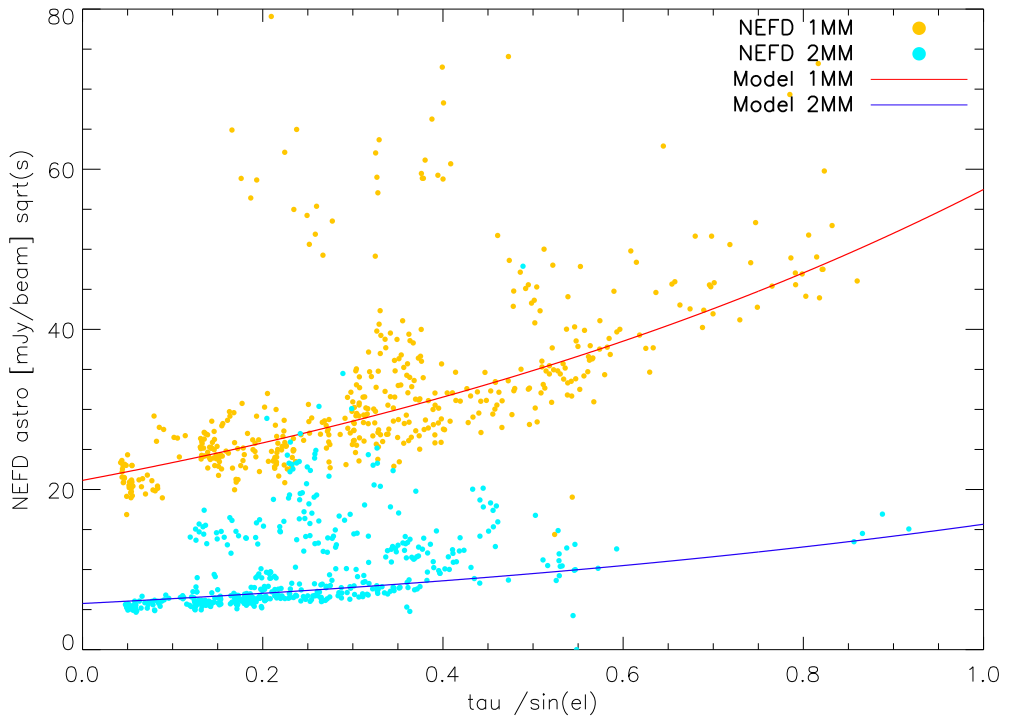


Figure 42: Astronomer NEFD as a function of atmospheric background for the 1 (orange dots) and 2 (cyan dots) mm channels. We also show the expected NEFD evolution with atmospheric background (red and blue curves)



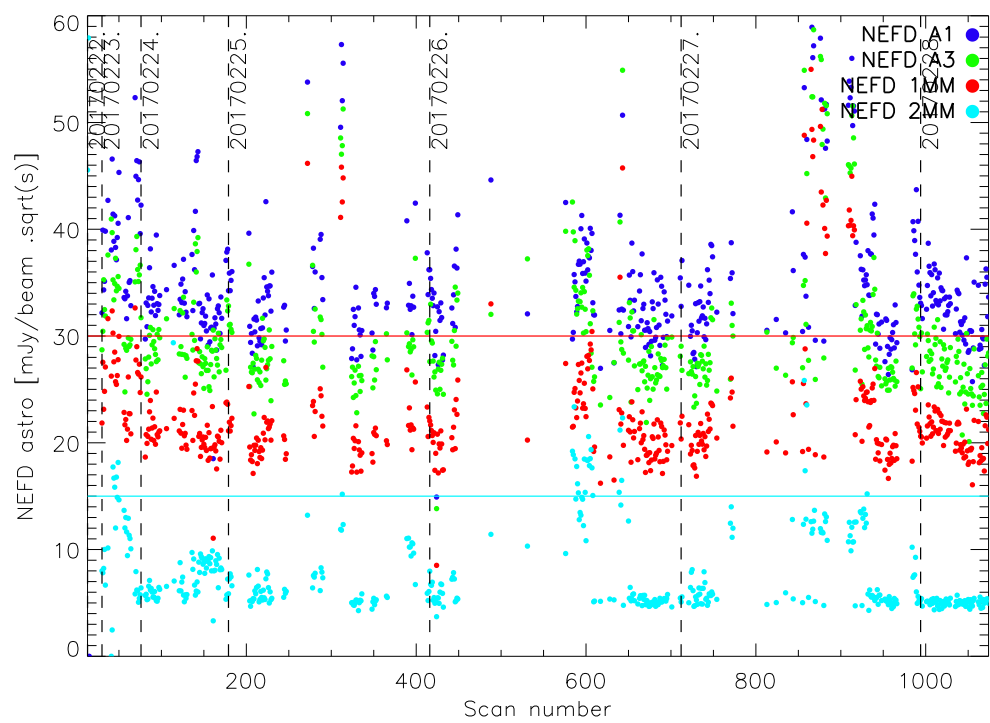


Figure 43: Evolution of the measured instrument NEFD across scans for N2R9.

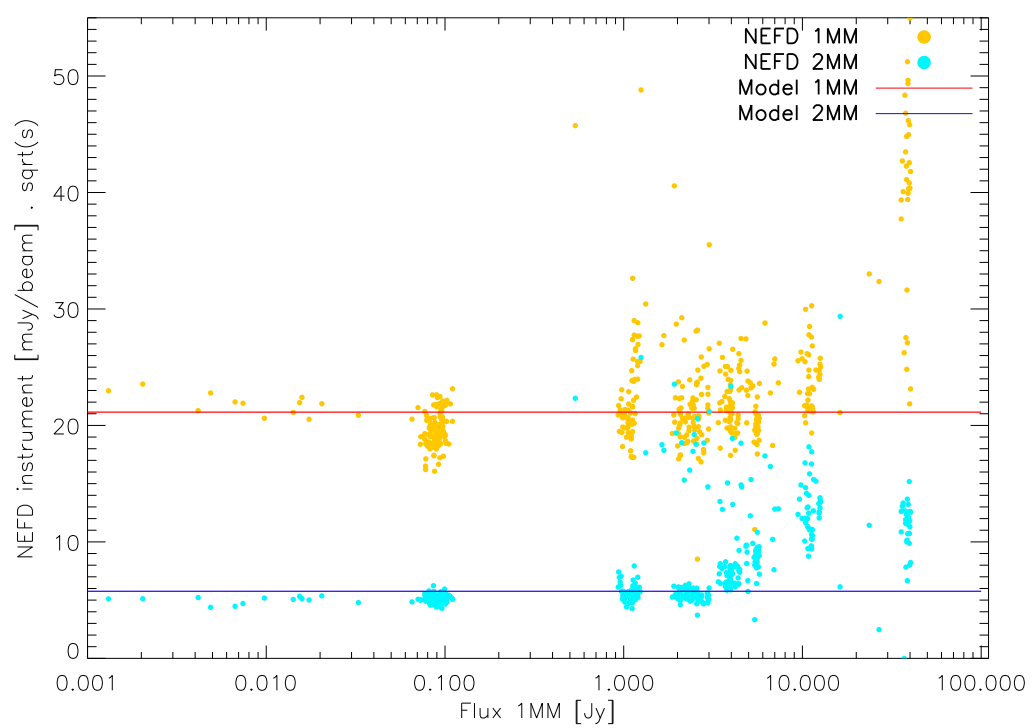


Figure 44: Measured instrument NEFD as a function of the flux of the source.

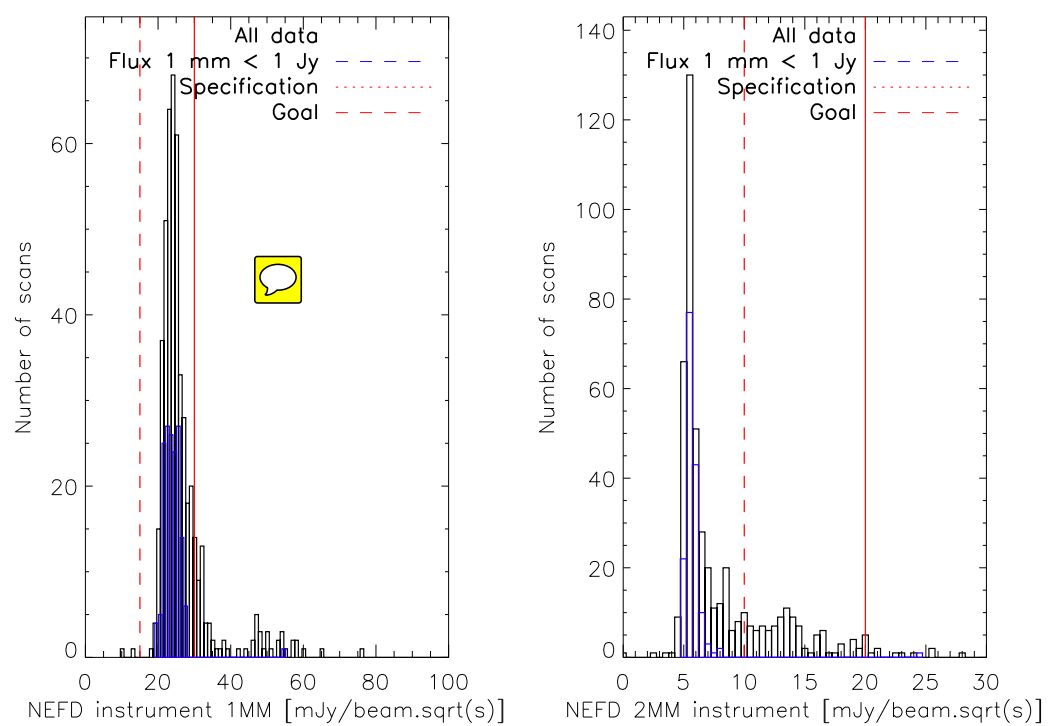


Figure 45: Histogram of the measured reference NEFD across the N2R9 for the 1 (right) and 2 (left) mm channels.

Table 9: Summary of the main characteristics describing the measured performances of NIKA2.

	Array 1	Array 3	Array 1&3	Array 2
Reference Wavelength [mm]	1.2	1.2	1.2	2.0
Reference Frequency [GHz]	260	260	260	150
Central Frequency [GHz]	255.5	257.8		151.6
Bandwidth [GHz]	47.8	45.7		42.1
Number of designed detectors	1140	1140		616
Number of valid detectors	952	961		553
Fraction of valid detectors [%]				
Effective FOV ^a [arcmin]	5.39	5.61		4.9
Pixel size in beam sampling unit [$F\lambda$]				
FWHM ^b [arcsec]	11.3 ± 0.2	11.2 ± 0.2	11.2 ± 0.1	17.7 ± 0.1
Beam efficiency ^c [%]				
rms of the FWHM on the FOV [%]				
rms calibration error [%]	4.5	6.6		5
Absolute calibration uncertainty [%]			5	
α noise integration in time ^d				
rms pointing error [arcsec]			< 3	
NEFD ^e [mJy \cdot s $^{1/2}$ /beam]	30 (15)	30 (15)	30 (15)	20 (10)
Mapping speed ^f [arcmin 2 /h/mJy 2]	302	454	775 (1184)	7542 (10861)

(a) Equivalent FOV covered by the valid detectors

(b) Full-width at half-maximum of the main beam modelled as a two-dimensional Gaussian fitted from sidelobe-masked beam maps.

(c) Ratio between the main beam power and the total beam power up to a radius of XXX arcsec

(d) Effective power law of noise reduction with integration time

(e) NEFD in typical IRAM good sky opacity condition: 2mm pwv, 60° elevation

(f) Average (best) mapping speed at zero opacity for the February 2017 observation campaign.

Table 10: Summary of the main characteristics describing the measured performances of NIKA2, as listed in MoU

	Array 1	Array 3	Array 1&3	Array 2
NEFD ^a [mJy · s ^{1/2} /beam]	30 (15)	30 (15)	30 (15)	20 (10)
Number of designed detectors	1140	1140		616
Number of valid detectors	952	961		553
Fraction of valid detectors [%]				
FWHM ^b [arcsec]	11.3 ± 0.2	11.2 ± 0.2	11.2 ± 0.1	17.7 ± 0.1
Effective FOV ^c [arcmin]	5.39	5.61		4.9
Pixel size in beam sampling unit [F λ]				

(a) NEFD in typical IRAM good sky opacity condition: 2mm pwv, 60° elevation

(b) Full-width at half-maximum of the main beam modelled as a two-dimensional Gaussian fitted from sidelobe-masked beam maps.

(c) Equivalent FOV covered by the valid detectors

Table 11: Summary of other NIKA2 performance characteristics either defined in the MoU or extracted from SL’s summary document

	Array 1	Array 3	Array 1&3	Array 2
Reference Wavelength [mm]	1.2	1.2	1.2	2.0
Reference Frequency [GHz]	260	260	260	150
Central Frequency [GHz]	255.5	257.8		151.6
Bandwidth [GHz]	47.8	45.7		42.1
Beam efficiency ^a [%]				
rms of the FWHM on the FOV [%]				
rms calibration error [%]	4.5	6.6		5
Absolute calibration uncertainty [%]			5	
α noise integration in time ^d				
rms pointing error [arcsec]			< 3	
Mapping speed ^b [arcmin ² /h/mJy ²]	302	454	775 (1184)	7542 (10861)

(a) Ratio between the main beam power and the total beam power up to a radius of XXX arcsec

(b) Average (best) mapping speed at zero opacity for the February 2017 observation campaign.